

# 1 Diapycnal mixing and tracer dispersion in a 2 terrain-following coordinate model

3 Noémie Schifano<sup>1</sup>, Clément Vic<sup>1</sup>, Jonathan Gula<sup>1,2,3</sup>, M. Jeroen Molemaker<sup>3</sup>,  
4 James C. McWilliams<sup>3</sup>

5 <sup>1</sup>Univ Brest, CNRS, Ifremer, IRD, Laboratoire d'Océanographie Physique et Spatiale (LOPS), IUEM,  
6 Plouzané, France

7 <sup>2</sup>Institut Universitaire de France (IUF), Paris, France

8 <sup>3</sup>Department of Atmospheric and Oceanic Sciences and Institute of Geophysics and Planetary Physics,  
9 University of California, Los Angeles, CA 90095-1565, United States

## 10 Key Points:

- 11 • Diapycnal mixing is quantified in realistic high-resolution simulations using pas-  
12 sive tracer experiments and online diagnostics of effective diapycnal mixing
- 13 • Effective diapycnal mixing is close to parameterized values over the abyssal plain  
but can be larger above steep ridge slopes
- 14 • Numerical mixing is minimized by smoothing topography and effective mixing aligns  
closely with parameterized mixing

---

Corresponding author: N. Schifano, [noemie.schifano@univ-brest.fr](mailto:noemie.schifano@univ-brest.fr)

17 **Abstract**

18 Diapycnal mixing, driven by small-scale turbulence, is crucial for global ocean circula-  
19 tion, particularly for the upwelling of deep water masses.

20 However, accurately representing diapycnal mixing in ocean models is challenging  
21 because numerical errors can introduce significant numerical mixing that complicates the  
22 overall mixing representation.

23 In this study, we explore the diapycnal mixing in a high-resolution regional model  
24 of the North Atlantic's subpolar gyre using the Coastal and Regional Ocean Commu-  
25 nity model (CROCO), a terrain-following coordinate model widely used for regional ap-  
26 plications.

27 Terrain-following coordinates may offer a more accurate representation of bound-  
28 ary currents than z-level or isopycnal coordinates, mainly because they provide a sim-  
29 pler and clearer bottom boundary condition. However, they can also cause more diapy-  
30 cnal mixing due to the vertical levels not aligning with isopycnals. This numerical mix-  
31 ing can be reduced by using an operator that rotates the mixing along isopycnal surfaces.

32 We explore challenging dynamical regimes involving energetic submesoscale mo-  
33 tions and high-frequency internal waves over the Reykjanes Ridge. We focus on how dif-  
34 ferent advection schemes and vertical resolutions affect numerical diapycnal mixing. Our  
35 approach includes online diagnostics of buoyancy fluxes and Tracer Release Experiments  
36 to quantify the effective mixing, which combines parameterized and numerical diapyc-  
37 nal mixing.

38 Our main results show that in flat regions, numerical mixing is minimal, and ef-  
39 fective diapycnal mixing is close to the parameterized values. However, in regions with  
40 steep topography, such as the Reykjanes Ridge, numerical mixing can locally significantly  
41 exceed parameterized mixing due to grid slope constraints imposed by the rotated mix-  
42 ing operator. While topography smoothing can mitigate this excessive mixing, it can also  
43 alter flow-topography interactions. In addition, while a higher vertical resolution reduces  
44 the numerical mixing induced by the vertical advection of the tracer, it can also increase  
45 numerical mixing in steep regions by introducing a stronger constraint on the grid slope.

46 These results underscore the complex trade-offs in managing numerical mixing in  
47 ocean models. Accurately representing diapycnal mixing requires balancing high reso-  
48 lution with the control of numerical errors. Effective management involves careful con-  
49 sideration of topographic smoothing and resolution adjustments.

50 **1 Introduction**

51 The low-frequency and large-scale ocean circulation is mostly adiabatic, as water  
52 masses move predominantly along surfaces of constant density, or isopycnals. However,  
53 diabatic processes, which involve mixing across isopycnals, are crucial for closing the gen-  
54 eral circulation (de Lavergne et al., 2022). This diapycnal mixing shapes the lower limb  
55 of the meridional overturning circulation (e.g., Stommel, 1958; Samelson & Vallis, 1997).  
56 Recent theories of the abyssal circulation insist on the role of diapycnal mixing, and its  
57 still partially uncovered space and time variability, in the upwelling of the heaviest wa-  
58 ter masses (e.g., reviewed in de Lavergne et al., 2022).

59 Yet, diapycnal mixing remains difficult to map globally and statistically, because  
60 its main driver is small-scale turbulence, which is patchy and intermittent by nature. The  
61 most accurate estimate of diapycnal mixing is obtained by microstructure (very high fre-  
62 quency) measurements of velocity shear (a review of the measurement techniques can  
63 be found in Frajka-Williams et al., 2022). Indirect techniques for measuring diapycnal  
64 mixing, such as Tracer Release Experiments (TRE), have been developed to assess the

intensity of mixing over different time and space scales (Ledwell & Watson, 1991). Direct and indirect measurements have revealed the very large variability of diapycnal mixing throughout the world's oceans (Ledwell et al., 1993, 2000; Naveira Garabato et al., 2004; Kunze et al., 2006; Waterhouse et al., 2014).

The main energy sources for diapycnal mixing are tides and winds (Munk & Wunsch, 1998). They generate internal gravity waves that travel through the ocean before breaking, triggering diapycnal mixing. Topographic wakes can also be a strong source of interior diapycnal mixing (Mashayek et al., 2024). In situ measurements have shown that the magnitude of diapycnal mixing varies by several orders of magnitude depending on the bathymetry (see, for example, Fig. 7 of Waterhouse et al. (2014)). Successive refinements in the knowledge of the physics and energetics of internal waves have led to the development of parameterizations of diapycnal mixing driven by internal waves, especially for global ocean circulation models that will not resolve them in a foreseeable future (e.g., Jayne & St Laurent, 2001; Olbers & Eden, 2013; de Lavergne et al., 2019, 2020; Alford, 2020).

In primitive-equation regional and global models that include tidal forcing and high-frequency atmospheric forcing, internal gravity waves and other small-scale instability processes that lead to diapycnal mixing can be partially represented (e.g., Zilberman et al., 2009; Arbic et al., 2010; Gula et al., 2016; Vic et al., 2018; Mazloff et al., 2020; Thakur et al., 2022). As a result, specific parameterizations for diapycnal mixing driven by internal waves are not typically employed. Instead, diapycnal mixing is parameterized using turbulent closures that bridge the gap between internal waves, small-scale instability processes, and actual mixing. For example, using the K-profile parameterization (KPP, Large et al., 1994), one assumes that the represented currents produce sufficient vertical shear to trigger KPP's Richardson-based mixing, and a background diffusivity value is set to cover internal waves not resolved by the model.

In addition to the parameterized mixing, advection schemes produce additional mixing, often undesired, sometimes called 'numerical' or 'spurious' mixing (Griffies et al., 1998, 2000; Lee et al., 2002; Hofmann & Morales Maqueda, 2006; Burchard & Rennau, 2008; Marchesiello et al., 2009; Hecht, 2010; Hill et al., 2012; Bracco et al., 2018; Megann, 2018). This numerical mixing is an important issue because it includes a diapycnal component that potentially exceeds the parameterized mixing, sometimes by several orders of magnitude (Bracco et al., 2018). Its intensity is determined by the accuracy of the advection schemes, the horizontal and vertical resolution, and the type of the coordinate system (geopotential, isopycnal, or terrain-following coordinates). Strategies have been designed to minimise the diapycnal part of the numerical mixing by rotating it along isoneutral surfaces (Griffies et al., 1998), with solutions specifically designed for terrain-following coordinates (Marchesiello et al., 2009; Lemarié et al., 2012). However, the impact of such solutions on the effective diapycnal mixing has rarely been quantified for regional submesoscale-permitting or submesoscale-resolving models, especially in the presence of tides and other high-frequency motions. If one wants to use a primitive equation model specifically to study diabatic processes, and their impact on water mass transformation and deep ocean circulation, one cannot ignore mixing due to advection schemes. Moreover, the simulated ocean dynamics is sensitive to the vertical resolution, which affects tracer spreading and has important consequences for water mass representation (Stewart et al., 2017; Xu et al., 2023).

In the present study, we aim to quantify the diapycnal mixing due to different advection schemes routinely used in the Coastal and Regional Ocean Community model (CROCO), based on the Regional Oceanic Modelling System (ROMS, A. F. Shchepetkin & McWilliams, 2005). We pay particular attention to how the advection schemes, in combination with different vertical resolutions, affect the representation of passive tracers.

We set up a regional configuration in the subpolar North Atlantic Gyre, which includes part of the Reykjanes Ridge and the Iceland Basin. This region is of particular interest because it is located at the gateway of dense water formation (Piron et al., 2017) and has several sources of turbulence due to strong wind events and flow-topography interactions (Vic et al., 2021). We use micro-structure measurements from cruises OVIDE08 (Ferron et al., 2014), RREX15 (Branellec & Thierry, 2016) and RREX17 (Branellec & Thierry, 2018) to verify the realism of the mixing parameterization used in the model. The numerical mixing is estimated using a novel ad hoc online diagnostic and passive tracer release experiments (TREs). While the former allows us to precisely quantify the pointwise extra mixing due to the numerical schemes, the latter are a useful tool to visually capture the specific features of each scheme, and also to independently quantify the amount of mixing experienced by a tracer over different physical and numerical conditions. We also argue that the tracers can be seen as localized patches of biological or geochemical material to illustrate how the tracers' behavior is affected by numerical choices.

The plan is as follows. In section 2, we present the model configuration and the set of simulations we designed to investigate the impact of numerical choices on diapycnal mixing. We also present the different methods used to quantify diapycnal mixing, online, and based on the TREs. In section 3, we present an overview of the simulated dynamics along with a comparison of the simulated mixing with in situ estimates from microstructure data. We then compare the different estimates of diapycnal mixing (parameterized vs diagnosed following the different methods) in different regions, over smooth vs steep and rough topography. The impact of the advection schemes on the tracer representation is illustrated. In section 4 we summarize the results and discuss the limitations of the methods as well as the implications of our findings.

## 2 Methods

### 2.1 Numerical set up

We perform three-dimensional realistic simulations using the ocean model CROCO (Auclair et al., 2022). CROCO has been developed on the basis of ROMS (A. F. Shchepetkin & McWilliams, 2005) and still shares a significant amount of code, in particular most of the numerical options detailed below. It solves the primitive equations and uses terrain-following (sigma) coordinates. We use the hydrostatic version of the code. The model domain covers part of the Reykjanes Ridge, south of Iceland, and part of the Iceland Basin to its east (Figure 3). The model grid has  $1000 \times 800$  points on the horizontal with a grid spacing of 800 m, and the number of vertical levels varies between 50 and 200 across the set of simulations (Section 2.2 and Table 1). The horizontal resolution is among the standards in the regional modelling community, and allows to resolve the mesoscales and partially resolve the submesoscales and the internal gravity wave continuum (e.g., Arbic, 2022). All simulations are run with a time step of 80 seconds.

The model bathymetry is based on the 15-second resolution Shuttle Radar Topography Mission dataset (SRTM15.PLUS, Tozer et al., 2019). The raw bathymetry is smoothed with a Gaussian kernel with a radius of 5 grid points to avoid steep gradients that could lead to pressure gradient errors (A. F. Shchepetkin & McWilliams, 2003). The steepness parameter does not exceed  $r = 0.2$  (Beckmann & Haidvogel, 1993).

Atmospheric forcing is provided at hourly resolution by the Climate Forecast System Reanalysis (CFSR, Saha et al., 2010). Initial and boundary conditions are provided by a parent simulation covering the entire Atlantic Ocean at 3-km resolution, GIGATL3 (Gula et al., 2021). The parent simulation includes barotropic and baroclinic tides. Thus, the tidal forcing is embedded in the boundary conditions at hourly resolution. We initialize the simulations in Aug 2008 and run them for 2 months.

The subgrid scale mixing is parameterised using the KPP scheme (Large et al., 1994).  
 165 KPP is a turbulent closure of scalars and momentum that provides the vertical eddy diffusivity coefficient  $K_{KPP}$ . In the surface and bottom layers, which are calculated based  
 166 on a critical bulk Richardson number,  $K_{KPP}$  is the product of the boundary layer thickness  $h_{bl}$ , a turbulent velocity scale  $w_S$  and a shape function  $G$ , both of which depend on  
 167 the vertical coordinate  $\sigma$ :

$$K_{KPP} = h_{bl} w_S(\sigma) G(\sigma). \quad (1)$$

In the interior, outside these layers,  $K_{KPP}$  is calculated as the sum of three processes: Background internal wave breaking, vertical shear instability, and convective instability. Background internal wave breaking is parameterized with a constant background diffusivity ( $K^w = 10^{-5} \text{ m}^2 \text{ s}^{-1}$ ).  
 171  
 172  
 173  
 174

Vertical shear instability is parameterized using the Richardson number  $Ri = N^2/S^2$ , where  $N^2$  is the buoyancy frequency squared and  $S^2 = (\frac{\partial u}{\partial z})^2 + (\frac{\partial v}{\partial z})^2$  is the squared vertical shear of the horizontal velocity, using the same formulation than in Large et al.  
 175 (1994):

$$K^S = \begin{cases} \nu^0 & Ri < 0 \\ \nu^0 \left[ 1 - \left( \frac{Ri}{Ric} \right)^2 \right]^3 & 0 < Ri < Ric \\ 0 & Ric < Ri \end{cases}$$

with a critical Richardson number  $Ric = 0.7$  and  $\nu^0 = 5 \times 10^{-3} \text{ m}^2 \text{ s}^{-1}$ . In case of convective instability ( $N^2 \leq 0$ ), an additional diffusivity  $K^C = 10^{-1} \text{ m}^2 \text{ s}^{-1}$  is added.  
 179  
 180

All of the simulations presented below use the same third order upwind scheme (UP3)  
 181 for momentum advection in the horizontal (A. F. Shchepetkin & McWilliams, 2005). Horizontal advection schemes for active tracers (potential temperature and salinity) are split  
 182 and rotated upstream biased schemes of the third (RSUP3) or fifth order (RSUP5) de-  
 183 pending on the experiments, with the rotation oriented along isoneutral surfaces (Lemarié  
 184 et al., 2012). The vertical advection of momentum and active tracers uses a fourth-order  
 185 centered parabolic spline reconstruction (SPLINES), with an adaptive, Courant-number-  
 186 dependent implicit scheme (A. F. Shchepetkin, 2015).  
 187  
 188

The advection of passive tracers uses either the same schemes as for active tracers (RSUP3 or RSUP5 in the horizontal, and SPLINES in the vertical) or a 5th-order Weighted Essentially Non-Oscillatory scheme (WENO5, Jiang & Shu, 1996) in all directions. The WENO5 scheme is a common choice for biogeochemical tracers, mainly because it limits oscillations and the negative concentrations (Figure 2). Therefore, it is important to assess how it affects numerical mixing as it would affect the global cycles of biogeochemical tracers. The different combinations of schemes for our sensitivity studies are summarized below.

## 197 2.2 Set of simulations

We focus here on two parameters that affect numerical mixing: the vertical resolution and the choice of advective schemes. The vertical resolution depends on the number of  $\sigma$ -levels and the local bathymetry (Figure 1). We tested the sensitivity of mixing in simulations with 50, 100 and 200 vertical levels. While the use of 50 levels (or less) has long been in the range of the community standards (e.g., Marchesiello et al., 2003; Penven et al., 2005), the use of  $\approx 100$  levels has become routine to better represent current-topography interactions (e.g., Molemaker et al., 2015; Gula et al., 2016, 2019; Vic et al., 2018). The use of 200 levels is significantly more computationally expensive, but, as shown in the results section, provides important improvements in the representation of passive tracers.  
 198  
 199  
 200  
 201  
 202  
 203  
 204  
 205  
 206  
 207

208 We use three combinations of advective schemes (listed in Table 1):

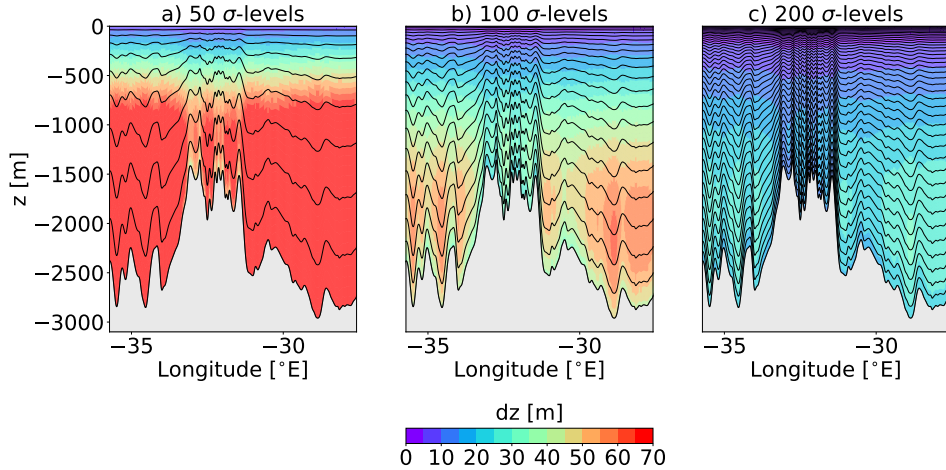


**Figure 1.** Vertical resolution [m] using (a) exp50-rsup5 (b) exp100-rsup5 and (c) exp200-rsup5. The vertical section is taken at the black dashed line in figure 3.

- The rsup3 combination uses RSUP3 in the horizontal and SPLINES in the vertical for active and passive tracers
- The rsup5 combination uses RSUP5 in the horizontal and SPLINES in the vertical for active and passive tracers
- The weno5 combination uses RSUP5 and SPLINES for active tracers, and WENO5 in the horizontal and vertical for passive tracers.

Each combination is run with 50, 100, and 200 vertical levels. Each simulation is labelled ‘ $\text{exp}i\text{-}j$ ’ where  $i \in \{50, 100, 200\}$  is the number of vertical levels and  $j \in \{\text{rsup3}, \text{rsup5}, \text{weno5}\}$  is the advective scheme combination.

An additional simulation, exp200-rsup5-smooth, is run with the rsup5 combination and a smoother bathymetry than in the baseline simulations. This choice is motivated by the result showing increased numerical mixing over steep topography. The hydrostatic consistency condition  $rx_1$  (sometimes called Haney number, Haney, 1991)) maximum value over the domain is  $\approx 6$  for exp200-rsup5-smooth and  $\approx 17$  for exp200-rsup5.

### 2.3 Online diagnostic of diapycnal diffusivity

We define the effective diapycnal mixing as the sum of the parameterized and the numerical (i.e., due to advection schemes) diapycnal mixing. Here we present how we diagnose the effective diapycnal diffusivity, called  $K_{eff}$  in this article, at each point in space and time during the model computation.

To do this, we first diagnose the temperature and salinity budgets, including all numerical sources of mixing. We use them to compute a buoyancy budget and in particular to isolate the non-advection buoyancy fluxes. Finally, we project the fluxes in the direction orthogonal to the local isopycnal surfaces (based on local adiabatic density gradients) to obtain an effective diffusivity. The different steps are detailed below.

We first diagnose non-advection tracer fluxes ( $\vec{F^T}, \vec{F^S}$ ) for the potential temperature  $T$  and salinity  $S$  by closing the following budgets:

**Table 1.** List of experiments with their characteristic numerical features

Configuration name	Number of $\sigma$ levels	Time step	Horizontal		Vertical		Horizontal		Vertical	
			advective scheme for momentum	advective scheme for momenta	advective scheme for active tracers	advective scheme for passive tracers	advective scheme for active tracers	advective scheme for passive tracers	advective scheme for active tracers	advective scheme for passive tracers
exp50-rsup3	50	80	up3	splines	rsup3	splines	rsup3	splines	rsup3	splines
exp100-rsup3	100	80	up3	splines	rsup3	splines	rsup3	splines	rsup3	splines
exp200-rsup3	200	80	up3	splines	rsup3	splines	rsup3	splines	rsup3	splines
exp50-rsup5	50	80	up3	splines	rsup5	splines	rsup5	splines	rsup5	splines
exp100-rsup5	100	80	up3	splines	rsup5	splines	rsup5	splines	rsup5	splines
exp200-rsup5	200	80	up3	splines	rsup5	splines	rsup5	splines	rsup5	splines
exp200-rsup5-smooth	200	80	up3	splines	rsup5	splines	rsup5	splines	rsup5	splines
exp50-weno5	50	80	up3	splines	rsup5	splines	rsup5	splines	rsup5	splines
exp100-weno5	100	80	up3	splines	rsup5	splines	rsup5	splines	rsup5	splines
exp200-weno5	200	80	up3	splines	rsup5	splines	rsup5	splines	rsup5	splines

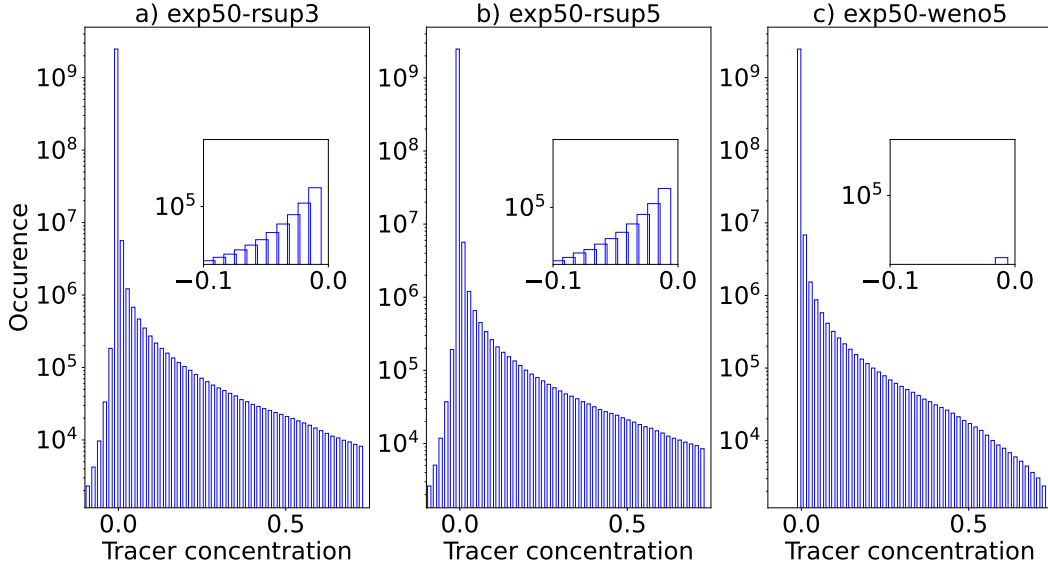


**Figure 2.** Histogram of tracer 1 concentration over 40 days for configurations: a) exp50-up3  
b) exp50-rsup5 and c) exp50-weno5

$$\frac{DT}{Dt} = \underbrace{T_t}_{T_{rate}} + \underbrace{\vec{u} \cdot \vec{\nabla} T}_{T_{adv}} = \underbrace{-\vec{\nabla} \cdot \vec{F}^T}_{T_{rhs}}$$

$$\frac{DS}{Dt} = \underbrace{S_t}_{S_{rate}} + \underbrace{\vec{u} \cdot \vec{\nabla} S}_{S_{adv}} = \underbrace{-\vec{\nabla} \cdot \vec{F}^S}_{S_{rhs}}$$

where the flux divergence on the r.h.s. includes contributions from: the parameterized vertical mixing from KPP, surface or bottom forcings, explicit horizontal mixing or implicit horizontal mixing due to the advection scheme (A. F. Shchepetkin & McWilliams, 2005), and other sources of numerical mixing such as implicit vertical advection (A. F. Shchepetkin, 2015), stabilisation of the isoneutral diffusive operator (Lemarié et al., 2012), or aspects related to the model time-stepping (A. Shchepetkin & McWilliams, 2008).

Non-advection buoyancy fluxes are then computed by combining the tracer fluxes:

$$\vec{F}^B = -g(-\alpha \vec{F}^T + \beta \vec{F}^S)$$

where the thermal expansion coefficient  $\alpha = -\frac{1}{\rho_0} \left( \frac{\partial \rho}{\partial T} \right)_S$  and the saline contraction coefficient  $\beta = \frac{1}{\rho_0} \left( \frac{\partial \rho}{\partial S} \right)_T$  are computed using a local 3d linearization of the equation of state of the model (A. Shchepetkin & McWilliams, 2011).

Finally, to get an effective diapycnal diffusivity, we project the buoyancy fluxes ( $\vec{F}^B$ ) in the direction orthogonal to the isopycnal surfaces  $\vec{n} = \frac{\vec{\nabla} b}{|\vec{\nabla} b|}$  (where  $\vec{\nabla} b$  are the adiabatic buoyancy gradients based on the definition of A. Shchepetkin and McWilliams (2011)) and divide by the norm of the same gradient:

$$K_{eff} = \vec{F}_B \cdot \frac{\vec{\nabla}b}{|\vec{\nabla}b|^2}$$

In the (ideal) case where the mixing is dominated by the vertical mixing parameterization ( $\vec{F}_B \approx (0, 0, K_{KPP} \frac{\partial b}{\partial z})$ ), and if we assume that the horizontal buoyancy gradients are small compared to the vertical stratification ( $|\frac{\partial b}{\partial x}|, |\frac{\partial b}{\partial y}| \ll |\frac{\partial b}{\partial z}|$ ), we should recover:  $K_{eff} = K_{KPP}$ .

Note that the method has two obvious limitations. The first is that it is only valid as long as essentially dissipative advective schemes are used. Using a scheme dominated by dispersive errors without explicit diffusivity would lead to an underestimation of the effective diffusivity. In addition, the diffusivity  $K_{eff}$  will be ill-defined in regions where the stratification vanishes and the norm of the adiabatic buoyancy gradient goes to zero.

However, a strong advantage is that we do not need a passive tracer patch to estimate  $K_{eff}$ , which allows us to analyse effective mixing in parts of the domain that do not depend on the tracer patch spreading. In section 3.5, we use the estimation of the online effective mixing  $K_{eff}$  to study the impact of the topography on the effective mixing over areas not covered by tracer patches.

## 2.4 Diagnosis of diapycnal diffusivity based on tracer release experiments

Independent of the online diagnosis of effective mixing, we use TREs to diagnose the effective diffusivity in the model. In addition to providing a quantitative estimate of mixing, numerical TRE visually illustrate the diffusive and dispersive effects of the schemes.

Two passive tracers are released in each simulation. Tracer 1 is released over the abyssal plain in the Iceland Basin and tracer 2 is released over the Reykjanes Ridge. We expect the contrasting dynamics in these regions (smooth topography vs. rough topography) to produce different levels of mixing. The initial distributions of the tracer patches are Gaussian in density space:

$$c_{(t=0)} = \exp\left(-\frac{r^2}{2\sigma_r^2}\right) \exp\left(-\frac{(\rho - \rho_{target})^2}{2\sigma_\rho^2}\right)$$

, where  $r = \sqrt{(x - x_C)^2 + (y - y_C)^2}$  and  $(x_C, y_C)$  is the location of the center of the patch,  $\rho_{target}$  is the initial target density,  $\sigma_r = 2$  km,  $\sigma_\rho = 0.01$  kg m<sup>-3</sup>. The initial location of the tracers was chosen to keep the tracer patches in the domain as long as possible. Figure 4 shows the release of the tracer 1 (panels a,e) and the tracer 2 (panels c,g) and how the tracer patches are distributed vertically and horizontally 15 days after the release (panels b,f and d,h).

Two different methods are used to diagnose the diapycnal diffusivity experienced by each tracer. There are presented in the following.

### 2.4.1 Taylor estimate of diffusivity

Taylor (1922) studied the evolution of a tracer with a concentration  $c$  that follows the equation  $\frac{\partial c}{\partial t} = \kappa \nabla^2 c$ , where  $\kappa$  is the turbulent diffusivity. The main result is that  $\kappa$  is related to the growth rate of the tracer concentration variance in the considered direction. To estimate the diapycnal diffusivity, oceanographers have considered the diapycnal direction. The estimated diffusivity  $K_{tr}$  can thus be written as:

$$K_{tr} = \frac{1}{2} \frac{1}{\langle |\nabla b|^2 \rangle} \frac{\partial}{\partial t} \langle (b - \langle b \rangle)^2 \rangle, \quad (2)$$

282 where  $b$  is buoyancy and  $\langle \cdot \rangle$  is the tracer-weighted averaging operator:

$$\langle \cdot \rangle = \frac{\int \int \int c dx dy dz}{\int \int \int b dx dy dz}, \quad (3)$$

283 and the integral is taken over the full model volume.

284 For a constant mixing rate, we should recover  $K_{tr} = \kappa$ . Recently, Ruan and Fer-  
285 rari (2021) revisited Taylor's theory in the general case where the mixing rate varies in  
286 space. In this case, the interpretation of  $K_{tr}$  is more complicated. In the present sim-  
287 ulations, KPP produces diapycnal mixing coefficients that rarely deviate from the back-  
288 ground value in the ocean interior. We therefore expect  $K_{tr}$  to be as close as possible  
289 to  $\kappa$  if no numerical mixing has been produced.

#### 290 2.4.2 A one-dimensional model of tracer spreading across isopycnals

291 We also use an alternative method to estimate the diapycnal diffusivity based on  
292 a one-dimensional model describing the tracer evolution in buoyancy space. This model  
293 has been widely used in field TREs (e.g., Ledwell & Watson, 1991) and in virtual TREs  
294 (Holmes et al., 2019). It reads:

$$\frac{\partial \bar{c}}{\partial t} + \left( \bar{w} - \overline{\frac{\partial K_{fit}}{\partial h}} \right) \frac{\partial \bar{c}}{\partial h} = \overline{K_{fit}} \frac{\partial^2 \bar{c}}{\partial h^2}, \quad (4)$$

295 where  $w$  is the vertical velocity and the overbar denotes an average over buoyancy classes  
296 at a given height  $h$  above the buoyancy class targeted at the tracer release. A mean strat-  
297 ification profile is used to convert between  $h$  and  $b$ . The diapycnal diffusivity  $\overline{K_{fit}}$  is as-  
298 sumed to be a linear function of  $h$ ,  $\overline{K_{fit}} = \overline{K_0} + h \overline{\frac{\partial K_{fit}}{\partial h}}$ , where  $K_0$  is the diapycnal dif-  
299 fusivity at the target buoyancy. We use the method and algorithm described in Appendix B  
300 in Holmes et al. (2019) to infer  $K_{fit}$ . Briefly, Equation 4 is discretized and a least-square  
301 method is used at each time step to find the three parameters  $\overline{K_0}$ ,  $\overline{w}$  and  $\overline{\frac{\partial K_{fit}}{\partial h}}$  that min-  
302 imize the distance between the 'observed'  $\bar{c}$  inferred from the simulation and the 1-d model  
303 prediction from the initial distribution.

## 304 3 Results

### 305 3.1 Overview of the simulated dynamics

306 We first present an overview of the dynamics in the region. The large-scale and mesoscale  
307 dynamics are qualitatively similar in all simulations, and we only show examples from  
308 only one simulation (exp200-rsup5).

309 Mesoscale currents are remarkably barotropic, with horizontal currents extending  
310 from below the surface mixed layer to the seafloor (Figures 5a and 5b), as is character-  
311 istic of high-latitude gyres (Le Corre et al., 2020). The vertical velocity ( $w$ ) patterns have  
312 smaller horizontal and vertical scales with large amplitudes throughout the whole wa-  
313 ter column (Figure 5c). It is largely the signature of energetic internal waves, either gen-  
314 erated by flow-topography interactions above the Reykjanes Ridge as internal tides or  
315 lee waves or by the strong wind events in the gyre (Vic et al., 2021). The stratification,  
316 represented by  $N^2$ , is enhanced in the thermocline and decreases smoothly with depth  
317 (Figure 5d). It is minimal in the surface and bottom mixed layers, with values eventu-  
318 ally reaching zero and locally becoming negative. The vertical shear of horizontal veloc-  
319 ity,  $S^2$ , is enhanced in the thermocline and in the boundary layers (Figure 5e). Distinct  
320 thin layers ( $\approx 100$  m, a few vertical grid points) of elevated shear are characteristic of in-  
321 ternal waves, especially near-inertial waves (Alford et al., 2016).

322 The Richardson number  $Ri = S^2/N^2$  compares the destabilizing strength of shear  
323 with the stabilizing effect of stratification. Regions of strong shear and weak stratifica-  
324 tion are prone to shear instability and mixing, these regions correspond to values of  $Ri$

less than the critical value  $Ri_c$  (Figure 5f). In the boundary layers we often have  $Ri < Ri_c$ , while in the interior  $Ri > Ri_c$  almost everywhere, except in some thin shear layers described above. Thus, in the interior, the resulting diffusivity coefficient computed by KPP,  $K_{KPP}$ , is predominantly equal to its background value of  $10^{-5} \text{ m}^2 \text{ s}^{-1}$  (Figure 5g). In the boundary layers,  $K_{KPP}$  reaches high values up to  $10^{-1} \text{ m}^2 \text{ s}^{-1}$  where convective instabilities occur. The isopycnals also experience a net sinking that seems to follow the topographic shape, suggesting the generation of Lee waves that propagate into the interior of the ocean.

To assess the realism of the parametrised mixing coefficients  $K_{KPP}$ , we compared them with microstructure estimates from three cruises: OVIDE08 (Ferron et al., 2014), RREX15 (Branellec & Thierry, 2016), and RREX17 (Branellec & Thierry, 2018). Microstructure-based estimates are computed following Osborn (1980):

$$\kappa = \Gamma \frac{\epsilon}{N^2} \quad (5)$$

where  $\Gamma = 0.2$  is the mixing efficiency,  $\epsilon$  is the turbulent energy dissipation and  $N^2$  is the stratification. Both  $\epsilon$  and  $N^2$  are estimated from probes mounted on a vertical microstructure profiler (instrument manufactured by Rockland Scientific International Inc.). Details of the processing can be found in Ferron et al. (2014). The three cruises sampled the same section across the Reykjanes Ridge (shown in Figure 3). All products are shown in Figure 6. Data are binned on the same vertical grid with 100 m bins to facilitate comparison. The in situ estimates all show contrasting profiles between the Reykjanes Ridge and the Iceland Basin. Over the ridge, mixing increases from below the thermocline ( $10^{-5} \text{ m}^2 \text{ s}^{-1}$ ) down to the bottom ( $10^{-4} \text{ m}^2 \text{ s}^{-1}$ ), which is typical of internal tide-driven mixing over mid-ocean ridges (Waterhouse et al., 2014). Over the abyssal plain in the Iceland Basin, mixing is reduced and is close to  $10^{-5} \text{ m}^2 \text{ s}^{-1}$  throughout the whole water column. Overall,  $K_{KPP}$  is close to  $\kappa$  in the ocean interior and off the ridge, but is smaller over the ridge in the  $\approx 1000$  m above the seafloor. The model likely misses some intensified mixing events associated with internal wave breaking over rough topography and does not generate enough vertical shear to reach low enough Richardson numbers. The effective mixing  $K_{eff}$  is close to the KPP mixing (and observations) off the ridge. But it is higher than the KPP mixing over the ridge (fig. 6a)), highlighting the presence of numerical mixing over topographic slopes, in regions showing increased in-situ diffusivities.

### 3.2 Parameterized vs effective mixing

Overall, the effective diffusivity  $K_{eff}$  is close to  $K_{KPP}$  (Figure 5h). However, it is significantly larger in areas located above the steepest slopes of the seafloor topography above the Reykjanes Ridge, over a depth extending from the seafloor to several hundred meters or more above. We quantified this discrepancy more systematically by computing some statistics of  $K_{eff}$  in two contrasting regions, above the ridge and above the abyssal plain of the Iceland Basin, for the simulations with 50, 100 and 200 levels (Figure 7). Overall, it confirms the impression that  $K_{eff}$  departs from  $K_{KPP}$  above the ridge in the lowermost 1000 m above the seafloor ( $10^{-4} \text{ m}^2 \text{ s}^{-1}$  vs  $10^{-5} \text{ m}^2 \text{ s}^{-1}$ ), but is close to  $K_{KPP}$  in the abyssal plain.

Above the abyssal plain, increasing the number of  $\sigma$ -levels slightly reduces the effective mixing. This is especially true when increasing the number of levels from 50 to 100. There is also a slight improvement when increasing the number of levels from 100 to 200, as effective and parameterized mixing become very comparable. However, there are differences between effective and parameterized mixing above the ridge, regardless of the resolution. Furthermore, the differences are not significantly reduced when increasing the number of levels from 100 to 200, and even increase in the lower 800 m.

The intensification of  $K_{eff}$  with increasing vertical resolution above the ridge is counterintuitive. In fact, this intensification is related to numerical constraints on the isoneutral rotation of the diffusive part of the RSUP3/5 operators (Lemarié et al., 2012). These limits consist of conditions on the maximum isopycnal slope  $\alpha_m$  and the maximum grid slope ratio  $s_m$  for which the diffusive part of the advection schemes can be rotated along isopycnals:

$$\alpha_m = \max\left(\frac{\partial\rho}{\partial x}/\frac{\partial\rho}{\partial z}, \frac{\partial\rho}{\partial y}/\frac{\partial\rho}{\partial z}\right) < \alpha_c = 0.05 \quad (6)$$

$$s_m = \max\left(\frac{|\Delta_x\rho|}{|\Delta_z\rho|}, \frac{|\Delta_y\rho|}{|\Delta_z\rho|}\right) < s_c = 1, \quad (7)$$

where  $\Delta_i$  represents the difference between neighboring grid points in the  $i$  direction. If  $\alpha_m > \alpha_c$  or  $s_m > s_c$ , the diffusion will be along a direction that is not strictly aligned with isopycnals. This results in numerical diapycnal diffusion. Figures 8d,e show  $s_m$ , and Figures 8g,h show  $\alpha_m$  in simulations exp50-rsup5 and exp200-rsup5. There is a clear contrast between the abyssal plain, where  $s_m < s_c$  and  $\alpha_m < \alpha_c$ , and the ridge, which has large areas with  $s_m > s_c$  and  $\alpha_m > \alpha_c$ . Two reasons can be given to explain these differences. First, the ridge seafloor topography has larger gradients, hence the larger grid aspect ratio throughout the water column. Second, the enhanced internal wave activity over the ridge means that isopycnal slopes may be locally steeper than in the rest of the domain. Overall, the grid points that do not satisfy Equations 6 or 7 are associated with enhanced  $K_{eff}$  (Figure 8). Also, while increasing the number of vertical levels does not directly change the isopycnal slope (Figure 8g vs Figure 8h), it changes the grid slope ratio (Figure 8d vs Figure 8e), which has the direct effect of further increasing  $K_{eff}$  (Figure 8a vs Figure 8b).

This is confirmed more quantitatively by looking at the time-averaged ratio between effective and parameterized mixing as a function of the isopycnal slope  $\alpha_m$  and the grid slope ratio  $s_m$  (Fig. 9). The ratio is systematically greater than one for points where isopycnal slope and grid slope ratio exceed their respective critical values. The grid slope ratio  $s_m$  is the most limiting constraint for most points as suggested in (Lemarié et al., 2012).

Another interesting feature that emerges from increasing the number of levels is the sharpening of the contrast between interior and boundary mixing. The bottom boundary layer is better defined in the 100-level and 200-level simulations than in the 50-level simulation. This is likely to have important implications for water mass transformation near the bottom (Baker et al., 2023). Quantitatively, we also find that the effective mixing converges at 100  $\sigma$ -levels above the ridge, but not above the abyssal plain. At a depth of 1500 meters, 100  $\sigma$ -levels correspond to a vertical resolution of  $\approx 25$  meters above the ridge and  $\approx 50$  meters above the abyssal plain (see fig. 1b). When 200  $\sigma$ -levels are used, the vertical resolution at 1500 meters depth reaches  $\approx 25$  meters also above the abyssal plain (see fig. 1c)).

### 3.3 Spreading of the passive tracers

We now examine what happens to the 2 passive tracers released in the simulation in the abyssal plain and above the ridge.

The tracer concentration 10 days after release for the tracer released over the abyssal plain (tracer 1) is shown in Figure 10 for the different simulations. The most striking feature is the dispersive patterns obtained at the lowest vertical resolution (50 levels) when using the upstream horizontal advection schemes (rsup3 and rsup5) in combination with the vertical advection scheme splines. This dispersion is associated with the hyperdiffusivity (Boyd, 1994; Jiménez, 1994). It is strongly reduced by doubling the number of vertical levels to 100, and further reduced with 200 levels. The weno5 scheme combination is more diffusive, and the difference is most significant with 50 levels. Increasing the

419 number of levels to 100 or 200 levels significantly improves the tracer representation by  
 420 reducing numerical diffusion.

421 The tracer concentration for the tracer released above the ridge (tracer 2) is shown  
 422 in Figure 11. Overall, the two tracers show the same characteristics with respect to the  
 423 advection schemes used. Importantly, the differences between the combinations of schemes  
 424 are most pronounced when 50 levels are used, and gradually disappear when 100 and 200  
 425 levels are used. The results in all cases seem to converge between 100 and 200 levels.

### 426 3.4 Numerical mixing above the abyssal plain

427 We now compare the parameterized diffusivity in the model ( $K_{KPP}$ ) with our dif-  
 428 ferent estimates for the diapycnal diffusivity: the effective diffusivity  $K_{eff}$  based on the  
 429 online buoyancy budget and the tracer-based diapycnal diffusivities  $K_{fit}$  and  $K_{tr}$  diag-  
 430 nosed from the tracer spreading across isopycnals (Section 2.4).

431 These different estimates are shown in Fig. 12 for tracer 1, released above the abyssal  
 432 plain.  $K_{KPP}$  and  $K_{eff}$  are weighted by the tracer concentration and can thus be inter-  
 433 preted as the average diffusivity coefficients seen by the tracer. Thus, while  $K_{KPP}$  should  
 434 represent the diffusivity experienced by the tracer in the absence of additional diffusiv-  
 435 ity due to the advection schemes,  $K_{eff}$  represents the actual, effective mixing, which is  
 436 the sum of the prescribed mixing (from KPP) and the numerical mixing due to the ad-  
 437 vection schemes. The four estimates are diagnosed for each time step over the first 15  
 438 days after tracer release, and box plots represent their distribution over this period.

439 Basically,  $K_{KPP}$  and  $K_{eff}$  are close to  $10^{-5} \text{ m}^2 \text{ s}^{-1}$  (background mixing in KPP)  
 440 in all simulations, regardless of the number of vertical levels and the combination of schemes.  
 441 This background value can be seen as the modeler's target diffusivity, which the mod-  
 442 eler wants to be as close as possible to the parameterized value.

443 The two tracer-based estimates show large differences with the effective and pa-  
 444 rameterized diffusivities at the coarser vertical resolution, with diffusivities up to two or-  
 445 ders of magnitude larger (comparable to what is seen in bracco2018, for example). Us-  
 446 ing 50 vertical levels, both tracers experienced large diffusivities, two orders of magni-  
 447 tude larger than the parameterized diffusivities. However, increasing the number of ver-  
 448 tical levels significantly reduces the mixing experienced by the tracers. Overall, doubling  
 449 the number of vertical levels from 50 to 100 reduces the diffusivity experienced by tracer 1  
 450 by an order of magnitude, and again when doubling from 100 to 200. This is true for all  
 451 the advection schemes used. With 50 levels,  $K_{tr}$  reaches median values of  $1-3 \times 10^{-3} \text{ m}^2 \text{ s}^{-1}$ ,  
 452 which are two orders of magnitude larger than the targeted diffusivity. With 200 levels,  
 453  $K_{tr}$  is reduced to  $1-4 \times 10^{-5} \text{ m}^2 \text{ s}^{-1}$ , much closer to the parameterized values.

454 For the same vertical resolution, the weno5 combination is on average 2-3 times more  
 455 diffusive than the rsup3 and rsup5 combinations. Even with 200 levels, the two tracer-  
 456 based estimates do not converge to the effective mixing diagnosed in the simulation. The  
 457 differences between rsup3 and rsup5 are small, although  $K_{tr}$  is slightly larger for rsup5.  
 458 While the dissipative part of the advection scheme is expected to be about two times smaller  
 459 for rsup5 (visible in the slightly smaller effective diffusivities), the dispersive effects are  
 460 stronger for the 5-th order scheme, leading to slightly larger tracer-based diffusivities.

461 Note that  $K_{fit}$ , which is expected to be comparable to  $K_{tr}$ , is much smaller for the  
 462 50- and 100-level simulations using rsup3 and rsup5. We attribute this discrepancy to  
 463 a limit of the 1-d fit method when using a coarse vertical grid resolution in the presence  
 464 of dispersive errors. Indeed, the 1-d distribution of the tracer in buoyancy space does  
 465 not smoothly fit a Gaussian distribution (Figure 13), a requirement for the method to  
 466 be reliable (Holmes et al., 2019). The difference between  $K_{tr}$  and  $K_{fit}$  is much smaller  
 467 for exp50-weno5, which uses a more diffusive scheme. The difference between  $K_{tr}$  and

468  $K_{fit}$  disappears for exp200-rsup3 and exp200-rsup5. This confirms the visual impres-  
 469 sion in Figure 10 that the dispersive effect of the upstream/splines combination disap-  
 470 pears with 200 levels.

471 Naively, we might have expected  $K_{tr}$  (and to lesser extent,  $K_{fit}$ ) to be closer to  
 472  $K_{eff}$  for the rsup3 and rsup5 simulations even with 50 and 100 levels. Indeed, these sim-  
 473 ulations use the same advection schemes for the active tracers, used to diagnose  $K_{eff}$ ,  
 474 and for the passive tracers. However, the initial gradients of the passive tracers are much  
 475 larger than the temperature and salinity gradients at comparable depths. This leads to  
 476 increased dispersion of the passive tracers, which ultimately leads to increased tracer vari-  
 477 ance in buoyancy space, hence the larger values of  $K_{tr}$  as compared to  $K_{eff}$ .

### 478 3.5 Numerical mixing above the ridge

479 Tracer 2 is released above the ridge, where we expect higher levels of numerical mix-  
 480 ing in the model, as seen in section . The tracer-weighted parameterised mixing  $K_{KPP}$   
 481 (Fig. ) is not much different than above the abyssal plain, and remains close to the back-  
 482 ground value ( $10^{-5} \text{ m}^2 \text{ s}^{-1}$ ), showing that tracer 2 does not enter the bottom bound-  
 483 ary layer. However, the effective mixing seen by tracer 2,  $K_{eff}$ , departs from  $K_{KPP}$  by  
 484 a factor of 2-3 for the 50-level simulations and by an order of magnitude for the 200-level  
 485 simulations. This enhancement is due to the slope limiters (see section ) and is confined  
 486 to above the ridge as shown in Figures 8a and 8b.

487 Similar conclusions as for tracer 1 can be drawn for the tracer-based diapycnal dif-  
 488 fusivities estimated for tracer 2. Specifically, for a given set of advection schemes, increas-  
 489 ing the vertical resolution reduces the tracer-based diffusivity (Figure 14) until it reaches  
 490 the effective mixing values. Using 50 levels is still too coarse for the fit method, and  $K_{fit}$   
 491 is much smaller than  $K_{tr}$ . However, with 100 and 200 levels, there is good agreement  
 492 between  $K_{fit}$  and  $K_{tr}$ , which gives us confidence in the relevance of using TREs to di-  
 493 agnose mixing.

494 Among the different sets of schemes used, the weno5 combination is still more dif-  
 495 fusive by a factor of 2 to 5 (depending on the vertical resolution) compared to rsup3 and  
 496 rsup5. Among the upstream biased schemes, rsup5 is slightly less diffusive than rsup3,  
 497 as expected.

### 498 3.6 Effect of smoothing topography

499 Since the largest numerical mixing occurs over the steepest topographic slopes, it  
 500 is tempting to further smooth the original topography in order to reduce numerical mix-  
 501 ing. We tested this workaround by using a smoothing Gaussian kernel with three times  
 502 the characteristic scale. We used this smoothed topography to run simulation exp200-  
 503 rsup5-smooth, based on exp200-rsup5, which is the simulation that produces the least  
 504 numerical mixing. Figure 15a,b,c shows the baseline bathymetry, the smoothed bathymetry,  
 505 and the difference between the two. The difference in the distribution of topographic slopes  
 506 between the baseline topography and the modified topography is shown in Figure 15d.  
 507 While the baseline topography contains a non-negligible number of grid points with slopes  
 508 greater than 10% and up to 20%, the modified topography has slopes limited to 11% and  
 509 only a handful of slopes greater than 10%. Visually, the large-scale topographic struc-  
 510 tures of the ridge are preserved (Figure 8b vs 8c).

511 The effect of increasing the smoothing can be seen directly in  $\alpha_m$  and  $s_m$ , which  
 512 are reduced over the steepest slopes of the ridge (Figures 8f and 8i). The fraction of grid  
 513 points with  $\alpha_m > \alpha_c$  and  $s_m > s_c$  is significantly reduced. As a result,  $K_{eff}$  decreases  
 514 and is much closer to the parameterised background value (Figure 8c).

515      The efficiency of smoothing the topography to reduce numerical mixing is well il-  
 516      lustrated and quantified by the TRE of tracer 2 released over the ridge (Figure 16). In  
 517      short,  $K_{eff}$ ,  $K_{fit}$  and  $K_{tr}$  are all reduced by an order of magnitude and converge to  $K_{KPP}$ .  
 518      Note that there is a physical effect of smoothing the topography that adds to the nu-  
 519      mercial effect, which is to reduce the energetic turbulence associated with flow-topography  
 520      interactions and, in particular, the generation of internal tides. Thus, the isopycnal slopes  
 521      above the ridge are reduced, which helps to reduce  $\alpha_m$ .

## 522      4 Summary and Discussion

523      In this study, we investigated the diapycnal mixing in a realistic high-resolution sim-  
 524      ulation using a terrain-following coordinate model (CROCO) in a regional domain over  
 525      the Reykjanes Ridge, including tides and high-frequency winds. In particular, we tested  
 526      the impact of some numerical choices, namely, the advection schemes and the vertical  
 527      resolution, on the amount of numerical diapycnal mixing in the interior of the ocean. We  
 528      implemented two types of diagnostics to estimate the effective diapycnal mixing in the  
 529      simulations, defined as the sum of the parameterized mixing and the numerical mixing.  
 530      First, we implemented an online diagnostic, based on the computation of buoyancy fluxes  
 531      across isopycnal surfaces at each time step of the model. In parallel, we tested an alter-  
 532      native and complementary method based on TREs (Holmes et al., 2019; Ruan & Fer-  
 533      rari, 2021).

534      We used 10 configurations that differ in the horizontal and vertical advection schemes  
 535      used and the number of vertical levels (Table 1). The results can be summarized as fol-  
 536      lows:

- 537      • Using standard numerical parameters for a submesoscale-permitting simulation  
 538      ( $\Delta x = 800$  m) over the Reykjanes Ridge, the dynamics do not generate signifi-  
 539      cant mixing in the interior by the KPP scheme, despite the intense internal wave  
 540      activity. Vertical shear, mostly driven by internal waves, remains too small to trig-  
 541      ger Richardson-based mixing. Therefore, the parameterized mixing is close to its  
 542      background value in the interior over most of the domain and slightly weaker than  
 543      the observed mixing. The parameterization fails to reproduce the contrast between  
 544      ridge and abyssal with intensified mixing in the lowest part of the water column  
 545      above the ridge. Nonetheless, the effective mixing is enhanced above the ridge, which  
 546      has a steeper seafloor topography. This led us to study these two regions separately.
- 547      • Over the abyssal plain, the effective mixing is close to the parameterized mixing,  
 548      i.e. there is no significant numerical mixing despite the presence of internal waves,  
 549      thanks to the isoneutral diffusive operator used for active tracers in the model.  
 550      However, over the ridge, in the presence of steeper slopes, the effective mixing is  
 551      an order of magnitude larger than the parameterized mixing when using standard  
 552      numerical parameters and topography treatment. This difference is explained by  
 553      the presence of steep slopes, and in particular a grid slope ratio (also called hy-  
 554      drostatic inconsistency number) larger than 1, which limits the efficiency of the  
 555      isoneutral diffusive operator.
- 556      • The numerical mixing can be greatly reduced by additional smoothing of the to-  
 557      polography to ensure values of the grid slope ratio less than 1. In this case, the ef-  
 558      fective mixing is very close to the parameterized mixing over the entire domain.
- 559      • The tracer-based diffusivity estimates are much larger than the effective and pa-  
 560      rameterized mixing of the model at low vertical resolutions. Using 50 levels, the  
 561      tracer-based diffusivities are two orders of magnitude larger than the effective mix-  
 562      ing ( $10^{-3}$  m $^2$  s $^{-1}$  vs  $10^{-5}$  m $^2$  s $^{-1}$ ). This is explained either by dispersive effects  
 563      in the vertical advection of the tracers when using a combination of RSUP3/5 in  
 564      the horizontal and SPLINES in the vertical, or by strong diffusive effects when us-  
 565      ing WENO5 schemes in the horizontal and vertical. Using 100 levels greatly re-

duces these effects and reduces tracer-based diffusivities by an order of magnitude. When 200 levels are used, the tracer-based diffusivity is further reduced, and converges to the effective diffusivity. We also find that WENO5 schemes are on average two to three times more diffusive than the combinations of RSUP3/5 in the horizontal and SPLINES in the vertical, regardless of the number of levels.

Reducing, or at least controlling, numerical mixing in global and regional ocean models has been a major concern of the community (e.g., Griffies et al., 2000; Burchard & Rennau, 2008; Marchesiello et al., 2009; Hill et al., 2012). Our study shows that it necessarily involves dilemmas. While increasing the vertical resolution actually reduces dispersive and/or diffusive effects related to the vertical advection and leads to a more realistic representation of tracers, it also increases numerical mixing through increasing the grid slope ratio beyond acceptable limits, which renders the isoneutral diffusive operator less effective.

Thus, if limiting the numerical mixing to values less than the parameterized mixing in the interior of the ocean is a priority, e.g. when performing long-term equilibration or studying water mass transformation, one must be very careful in controlling the numerical mixing. An obvious solution is to further smooth the topography to ensure that the grid slope ratio remains of order one most of the time. It is not possible to compute the grid slope ratio *a priori*, without knowledge of the isopycnal slopes. However, this is largely achieved in practice by keeping the hydrostatic consistency condition close to unity for most of the domain (Fig. 9).

The downside is that smoothing the topography would also change the flow-topography interactions, since small-scale topographic features are important for converting barotropic tides into high-mode internal waves (de Lavergne et al., 2020) or for generating submesoscale instabilities (Gula et al., 2016). A promising solution to these problems might be the Brinkman penalization approach (Debreu et al., 2020, 2022), which allows to account for steep topographic slopes without increasing the grid slope ratio excessively.

A time filter can be added to the isoneutral slope calculation to limit possible numerical instabilities due to the nonlinearity of the equation of state in certain regimes (Griffies et al., 1998). This was not used in the experiments presented here, and no evidence of numerical instabilities related to isoneutral diffusion was found. However, we performed an additional experiment using exponential time smoothing with a time scale of 1 day (the default value in CROCO), which is shown in the appendix Appendix A. Even with a time scale as small as 1 day, it still leads to a noticeable increase in the numerical diffusivity due to the presence of high-frequency processes and fast isopycnal oscillations, as is the case here.

## 602 Appendix A Test with a isoneutral slope temporal filter and a cen- 603 tered advective scheme (C4)

604 Here we present some additional tests that we performed. We compare the exp100-  
605 rsup3 configuration presented above with two additional configurations:

- 606 • exp100-rsup3-filt, which is the same configuration as exp100-rsup3 with an addi-  
607 tional temporal filter that modifies the isoneutral slopes. This filter is activated  
608 by the "TS\_MIX\_ISO\_FILT" key in CROCO. It is an exponential smoothing with  
609 a time scale of 1 day;
- 610 • exp100-c4, which uses a fourth-order centered advective scheme (C4) for the hor-  
611 izontal advection of the tracers, with no additional diffusivity added. The rest of  
612 the configuration is identical to exp100-rsup3.

Using the time filter, we see that the effective mixing increases by a factor of 3 to 5 over the abyssal plain and the ridge (Fig. A1). The 1-day time scale is large enough to suppress isopycnal oscillations due to high-frequency processes. We also tested a time scale of 3 hours (not shown) and still observed an increase in effective diffusivity compared to the case with no time filtering.

The use of a centered advective scheme for tracer advection without diffusivity would be considered a bad numerical practice, as it is expected to lead to strong dispersive errors. And this is exactly what we observe here. The tracer-based diffusivities are much higher for both tracers than for any other configuration, leading to a much larger dispersion of the tracer cloud and extra diapycnal diffusivities. Above the abyssal plain, the effective diffusivity is very small because the method does not allow for dispersive effects. Above the ridge, the effective mixing is stronger in exp100-c4 compared to exp100-rsup3 only because the tracer penetrates inside the lower boundary layer.

## Appendix B Open Research

AGU requires an Availability Statement for the underlying data needed to understand, evaluate, and build upon the reported research at the time of peer review and publication.

Authors should include an Availability Statement for the software that has a significant impact on the research. Details and templates are in the Availability Statement section of the Data and Software for Authors Guidance: <https://www.agu.org/Publish-with-AGU/Publish/Author-Resources/Data-and-Software-for-Authors#availability>

It is important to cite individual datasets in this section and, and they must be included in your bibliography. Please use the type field in your bibtex file to specify the type of data cited. Some options include Dataset, Software, Collection, Computation-alNotebook. Ex:

```
638
639 @misc{https://doi.org/10.7283/633e-1497,
640   doi = {10.7283/633E-1497},
641   url = {https://www.unavco.org/data/doi/10.7283/633E-1497},
642   author = {de Zeeuw-van Dalfsen, Elske and Sleeman, Reinoud},
643   title = {KNMI Dutch Antilles GPS Network - SAB1-St_Johns_Saba_NA P.S.},
644   publisher = {UNAVCO, Inc.},
645   year = {2019},
646   type = {dataset}
647 }
648
```

For physical samples, use the IGSN persistent identifier, see the International Geo Sample Numbers section: <https://www.agu.org/Publish-with-AGU/Publish/Author-Resources/Data-and-Software-for-Authors#IGSN>

## Acknowledgments

The authors would like to acknowledge Bruno Ferron for the in-situ data from campaigns RREX15, RREX17 and OVIDE08. We also would like to acknowledge Ryan Holmes for sharing his code to compute the diffusivities  $K_{fit}$ . This work was supported by the French National Agency for Research (ANR) through the project DEEPER (ANR-19-CE01-0002-01), by the Office of Naval Research (ONR grant N00014-23-1-2226), and by ISblue project, Interdisciplinary graduate school for the blue planet (ANR-17-EURE-0015) and co-funded by a grant from the French government under the program "Investissements d'Avenir"

660 embedded in France 2030. Simulations were performed using HPC resources from GENCI-  
 661 TGCC (Grants 2022-A0090112051), and from HPC facilities DATARMOR of “Pôle de  
 662 Calcul Intensif pour la Mer” at Ifremer Brest France.

## 663 References

- 664 Alford, M. H. (2020). Global calculations of local and remote near-inertial-wave dis-  
 665 sipation. *Journal of Physical Oceanography*, 50(11), 3157–3164. doi: 10.1175/  
 666 JPO-D-20-0106.1
- 667 Alford, M. H., MacKinnon, J. A., Simmons, H. L., & Nash, J. D. (2016). Near-  
 668 inertial internal gravity waves in the ocean. *Annu. Rev. Mar. Sci.*, 8, 95–123.  
 669 doi: 10.1146/annurev-marine-010814-015746
- 670 Arbic, B. K. (2022). Incorporating tides and internal gravity waves within global  
 671 ocean general circulation models: A review. *Progress in Oceanography*, 102824.  
 672 doi: 10.1016/j.pocean.2022.102824
- 673 Arbic, B. K., Wallcraft, A. J., & Metzger, E. J. (2010). Concurrent simulation of  
 674 the eddying general circulation and tides in a global ocean model. *Ocean Mod-  
 675 ellng*, 32(3-4), 175–187. doi: 10.1016/j.ocemod.2010.01.007
- 676 Auclair, F., Benshila, R., Bordois, L., Boutet, M., Brémond, M., Caillaud, M., ...  
 677 Theetten, S. (2022, December). *Coastal and regional ocean community model*.  
 678 Zenodo. Retrieved from <https://doi.org/10.5281/zenodo.7415343> doi:  
 679 10.5281/zenodo.7415343
- 680 Baker, L., Mashayek, A., & Naveira Garabato, A. (2023). Boundary upwelling of  
 681 Antarctic Bottom Water by topographic turbulence. *AGU Advances*, 4(5),  
 682 e2022AV000858. doi: 10.1029/2022AV000858
- 683 Beckmann, A., & Haidvogel, D. B. (1993). Numerical simulation of flow around a  
 684 tall isolated seamount. part i: Problem formulation and model accuracy. *Jour-  
 685 nal of Physical Oceanography*, 23(8), 1736–1753.
- 686 Boyd, J. P. (1994). Hyperviscous shock layers and diffusion zones: Monotonicity,  
 687 spectral viscosity, and pseudospectral methods for very high order differential  
 688 equations. *Journal of Scientific Computing*, 9(1), 81–106. Retrieved from  
 689 <https://doi.org/10.1007/BF01573179> doi: 10.1007/BF01573179
- 690 Bracco, A., Choi, J., Kurian, J., & Chang, P. (2018). Vertical and horizontal reso-  
 691 lution dependency in the model representation of tracer dispersion along the  
 692 continental slope in the northern gulf of mexico. *Ocean Modelling*, 122, 13–25.  
 693 doi: <https://doi.org/10.1016/j.ocemod.2017.12.008>
- 694 Branellec, P., & Thierry, V. (2016). Rrex 2015. ctd-o2 data report.
- 695 Branellec, P., & Thierry, V. (2018). *Rrex 2017. ctd-o2 data report, rap. int* (Tech.  
 696 Rep.). LOPS/18-04, <https://doi.org/10.13155/58074>.
- 697 Burchard, H., & Rennau, H. (2008). Comparative quantification of physically and  
 698 numerically induced mixing in ocean models. *Ocean Modelling*, 20(3), 293–311.  
 699 doi: 10.1016/j.ocemod.2007.10.003
- 700 Debreu, L., Kevlahan, N.-R., & Marchesiello, P. (2020). Brinkman volume penaliza-  
 701 tion for bathymetry in three-dimensional ocean models. *Ocean Modelling*, 145,  
 702 101530. Retrieved from <https://www.sciencedirect.com/science/article/pii/S146350031930174X> doi: <https://doi.org/10.1016/j.ocemod.2019.101530>
- 703 Debreu, L., Kevlahan, N.-R., & Marchesiello, P. (2022). Improved gulf stream  
 704 separation through brinkman penalization. *Ocean Modelling*, 179, 102121.  
 705 Retrieved from <https://www.sciencedirect.com/science/article/pii/S1463500322001354> doi: <https://doi.org/10.1016/j.ocemod.2022.102121>
- 706 de Lavergne, C., Falahat, S., Madec, G., Roquet, F., Nylander, J., & Vic, C. (2019).  
 707 Toward global maps of internal tide energy sinks. *Ocean Modell.*, 137, 52–75.  
 708 doi: 10.1016/j.ocemod.2019.03.010
- 709 de Lavergne, C., Groeskamp, S., Zika, J., & Johnson, H. L. (2022). The role of mix-  
 710 ing in the large-scale ocean circulation. In *Ocean mixing* (pp. 35–63). Elsevier.
- 711

- 713 doi: <https://doi.org/10.1016/B978-0-12-821512-8.00010-4>
- 714 de Lavergne, C., Vic, C., Madec, G., Roquet, F., Waterhouse, A., Whalen, C.,  
 715 ... Hibiya, T. (2020). A parameterization of local and remote tidal  
 716 mixing. *Journal of Advances in Modeling Earth Systems*, 12(5). doi:  
 717 10.1029/2020MS002065
- 718 Ferron, B., Kokoszka, F., Mercier, H., & Lherminier, P. (2014). Dissipation rate  
 719 estimates from microstructure and finescale internal wave observations along  
 720 the A25 Greenland–Portugal OVIDE line. *Journal of Atmospheric and Oceanic  
 721 Technology*, 31(11), 2530–2543.
- 722 Frajka-Williams, E., Brearley, J. A., Nash, J. D., & Whalen, C. B. (2022). New tech-  
 723 nological frontiers in ocean mixing. In *Ocean mixing* (pp. 345–361). Elsevier.
- 724 Griffies, S. M., Gnanadesikan, A., Pacanowski, R. C., Larichev, V. D., Dukow-  
 725 icz, J. K., & Smith, R. D. (1998). Isoneutral diffusion in a z-coordinate  
 726 ocean model. *Journal of Physical Oceanography*, 28(5), 805 - 830. Retrieved  
 727 from [https://journals.ametsoc.org/view/journals/phoc/28/5/1520-0485\\_1998\\_028\\_0805\\_idiazc\\_2.0.co\\_2.xml](https://journals.ametsoc.org/view/journals/phoc/28/5/1520-0485_1998_028_0805_idiazc_2.0.co_2.xml) doi: 10.1175/1520-0485(1998)028<0805:IDIAZC>2.0.CO;2
- 728 Griffies, S. M., Pacanowski, R. C., & Hallberg, R. W. (2000). Spurious di-  
 729 apycnal mixing associated with advection in a z-coordinate ocean model.  
*Monthly Weather Review*, 128(3), 538–564. doi: [https://doi.org/10.1175/1520-0493\(2000\)128<0538:SDMAWA>2.0.CO;2](https://doi.org/10.1175/1520-0493(2000)128<0538:SDMAWA>2.0.CO;2)
- 730 Gula, J., Blacic, T. M., & Todd, R. E. (2019). Submesoscale coherent vortices in the  
 731 Gulf Stream. *Geophysical Research Letters*, 46(5), 2704–2714. doi: 10.1029/732 2019GL081919
- 733 Gula, J., Molemaker, M. J., & McWilliams, J. C. (2016). Topographic generation of  
 734 submesoscale centrifugal instability and energy dissipation. *Nat. Commun.*, 7.  
 735 doi: 10.1038/ncomms12811
- 736 Gula, J., Theetten, S., Cambon, G., & Roullet, G. (2021, June). *Description of the  
 737 gigatl simulations*. Zenodo. Retrieved from <https://doi.org/10.5281/zenodo.4948523> doi: 10.5281/zenodo.4948523
- 738 Haney, R. L. (1991). On the pressure gradient force over steep topography  
 739 in sigma coordinate ocean models. *Journal of Physical Oceanography*,  
 740 21(4), 610 - 619. Retrieved from [https://journals.ametsoc.org/view/journals/phoc/21/4/1520-0485\\_1991\\_021\\_0610\\_otpgfo\\_2.0.co\\_2.xml](https://journals.ametsoc.org/view/journals/phoc/21/4/1520-0485_1991_021_0610_otpgfo_2.0.co_2.xml) doi:  
 741 10.1175/1520-0485(1991)021<0610:OTPGFO>2.0.CO;2
- 742 Hecht, M. W. (2010). Cautionary tales of persistent accumulation of numerical error:  
 743 Dispersive centered advection. *Ocean Modelling*, 35(3), 270–276. doi: 10.1016/j.ocemod.2010.07.005
- 744 Hill, C., Ferreira, D., Campin, J.-M., Marshall, J., Abernathey, R., & Barrier, N.  
 745 (2012). Controlling spurious diapycnal mixing in eddy-resolving height-  
 746 coordinate ocean models—insights from virtual deliberate tracer release ex-  
 747 periments. *Ocean Modelling*, 45, 14–26. doi: 10.1016/j.ocemod.2011.12.001
- 748 Hofmann, M., & Morales Maqueda, M. (2006). Performance of a second-order  
 749 moments advection scheme in an ocean general circulation model. *Journal  
 750 of Geophysical Research: Oceans*, 111(C5). doi: <https://doi.org/10.1029/2005JC003279>
- 751 Holmes, R. M., de Lavergne, C., & McDougall, T. J. (2019). Tracer transport within  
 752 abyssal mixing layers. *Journal of Physical Oceanography*, 49(10), 2669–2695.  
 753 doi: <https://doi.org/10.1175/JPO-D-19-0006.1>
- 754 Jayne, S. R., & St Laurent, L. C. (2001). Parameterizing tidal dissipation over  
 755 rough topography. *Geophysical Research Letters*, 28(5), 811–814. doi: 10.1029/756 2000GL012044
- 757 Jiang, G.-S., & Shu, C.-W. (1996). Efficient implementation of weighted  
 758 eno schemes. *Journal of Computational Physics*, 126(1), 202-228. Retrieved  
 759 from <https://www.sciencedirect.com/science/article/pii/S0021999196900011>

- 768 S0021999196901308 doi: <https://doi.org/10.1006/jcph.1996.0130>
- 769 Jiménez, J. (1994). Hyperviscous vortices. *Journal of Fluid Mechanics*, 279,  
770 169–176. doi: 10.1017/S0022112094003861
- 771 Kunze, E., Firing, E., Hummon, J. M., Chereskin, T. K., & Thurnherr, A. M.  
772 (2006). Global abyssal mixing inferred from lowered adcp shear and ctd  
773 strain profiles. *Journal of Physical Oceanography*, 36(8), 1553–1576. doi:  
774 <https://doi.org/10.1175/JPO2926.1>
- 775 Large, W. G., McWilliams, J. C., & Doney, S. C. (1994). Oceanic vertical mixing: A  
776 review and a model with a nonlocal boundary layer parameterization. *Reviews  
777 of geophysics*, 32(4), 363–403. doi: <https://doi.org/10.1029/94RG01872>
- 778 Le Corre, M., Gula, J., & Trégouier, A.-M. (2020). Barotropic vorticity balance of  
779 the North Atlantic subpolar gyre in an eddy-resolving model. *Ocean Science*,  
780 16(2), 451–468. doi: 10.5194/os-16-451-2020
- 781 Ledwell, J. R., Montgomery, E., Polzin, K., St Laurent, L., Schmitt, R., & Toole, J.  
782 (2000). Evidence for enhanced mixing over rough topography in the abyssal  
783 ocean. *Nature*, 403(6766), 179–182.
- 784 Ledwell, J. R., & Watson, A. J. (1991). The santa monica basin tracer experiment:  
785 A study of diapycnal and isopycnal mixing. *Journal of Geophysical Research: Oceans*, 96(C5), 8695–8718.
- 786 Ledwell, J. R., Watson, A. J., & Law, C. S. (1993). Evidence for slow mixing  
787 across the pycnocline from an open-ocean tracer-release experiment. *Nature*,  
788 364(6439), 701–703.
- 789 Lee, M.-M., Coward, A. C., & Nurser, A. G. (2002). Spurious diapycnal mixing of  
790 the deep waters in an eddy-permitting global ocean model. *Journal of physical  
791 oceanography*, 32(5), 1522–1535.
- 792 Lemarié, F., Debreu, L., Shchepetkin, A., & Mcwilliams, J. C. (2012). On the stabil-  
793 ity and accuracy of the harmonic and biharmonic isoneutral mixing operators  
794 in ocean models. *Ocean Modell.*, 52, 9–35. doi: 10.1016/j.ocemod.2012.04.007
- 795 Marchesiello, P., Debreu, L., & Couvelard, X. (2009). Spurious diapycnal mixing in  
796 terrain-following coordinate models: The problem and a solution. *Ocean Mod-  
797 elling*, 26(3-4), 156–169. doi: 10.1016/j.ocemod.2008.09.004
- 798 Marchesiello, P., McWilliams, J., & Shchepetkin, A. (2003). Equilibrium structure  
799 and dynamics of the California Current System. *J. Phys. Oceanogr.*, 33(4),  
800 753–783. doi: 10.1175/1520-0485(2003)33<753:ESADOT>2.0.CO;2
- 801 Mashayek, A., Gula, J., Baker, L. E., Garabato, A. C. N., Cimoli, L., Riley, J. J.,  
802 & de Lavergne, C. (2024). On the role of seamounts in upwelling deep-ocean  
803 waters through turbulent mixing. *Proceedings of the National Academy of  
804 Sciences*, 121(27), e2322163121. Retrieved from <https://www.pnas.org/doi/abs/10.1073/pnas.2322163121> doi: 10.1073/pnas.2322163121
- 805 Mazloff, M. R., Cornuelle, B., Gille, S. T., & Wang, J. (2020). The importance of  
806 remote forcing for regional modeling of internal waves. *Journal of Geophysical  
807 Research: Oceans*, 125(2), e2019JC015623. doi: 10.1029/2019JC015623
- 808 Megann, A. (2018). Estimating the numerical diapycnal mixing in an eddy-  
809 permitting ocean model. *Ocean Modelling*, 121, 19–33. doi: <https://doi.org/10.1016/j.ocemod.2017.11.001>
- 810 Molemaker, M. J., McWilliams, J. C., & Dewar, W. K. (2015). Submesoscale  
811 instability and generation of mesoscale anticyclones near a separation of  
812 the California Undercurrent. *J. Phys. Oceanogr.*, 45(3), 613–629. doi:  
813 10.1175/JPO-D-13-0225.1
- 814 Munk, W., & Wunsch, C. (1998). Abyssal recipes II: Energetics of tidal and wind  
815 mixing. *Deep Sea Research Part I: Oceanographic Research Papers*, 45(12),  
816 1977–2010.
- 817 Naveira Garabato, A. C., Polzin, K. L., King, B. A., Heywood, K. J., & Visbeck, M.  
818 (2004). Widespread intense turbulent mixing in the Southern Ocean. *Science*,  
819 303(5655), 210–213.

- 823 Olbers, D., & Eden, C. (2013). A global model for the diapycnal diffusivity in-  
 824 duced by internal gravity waves. *Journal of Physical Oceanography*, 43(8),  
 825 1759–1779.
- 826 Osborn, T. R. (1980). Estimates of the local rate of vertical diffusion from dissipa-  
 827 tion measurements. *Journal of physical oceanography*, 10(1), 83–89.
- 828 Penven, P., Echevin, V., Pasapera, J., Colas, F., & Tam, J. (2005). Average cir-  
 829 culation, seasonal cycle, and mesoscale dynamics of the Peru Current Sys-  
 830 tem: A modeling approach. *J. Geophys. Res.*, 110(C10), C10021. doi:  
 831 10.1029/2005JC002945
- 832 Piron, A., Thierry, V., Mercier, H., & Caniaux, G. (2017). Gyre-scale deep con-  
 833 vection in the subpolar north atlantic ocean during winter 2014–2015. *Geo-*  
 834 *physical Research Letters*, 44(3), 1439–1447. doi: <https://doi.org/10.1002/2016GL071895>
- 835 Ruan, X., & Ferrari, R. (2021). Diagnosing diapycnal mixing from passive trac-  
 836 ers. *Journal of Physical Oceanography*, 51(3), 757–767. doi: [https://doi.org/10.1175/JPO-D-20-0194.1](https://doi.org/10.1175/10.1175/JPO-D-20-0194.1)
- 837 Saha, S., Moorthi, S., Pan, H.-L., Wu, X., Wang, J., Nadiga, S., ... others (2010).  
 838 The ncep climate forecast system reanalysis. *Bulletin of the American  
 839 Meteorological Society*, 91(8), 1015–1058. doi: <https://doi.org/10.1175/2010BAMS3001.1>
- 840 Samelson, R., & Vallis, G. K. (1997). Large-scale circulation with small diapycnal  
 841 diffusion: The two-thermocline limit. *Journal of Marine Research*, 55(2), 223–  
 842 275.
- 843 Shchepetkin, A., & McWilliams, J. C. (2008). Computational kernel algorithms for  
 844 finescale, multi-process, long-time oceanic simulations. *Handb. Numer. Anal.*,  
 845 14, 121–183.
- 846 Shchepetkin, A., & McWilliams, J. C. (2011). Accurate Boussinesq modeling with a  
 847 practical, "stiffened" equation of state. , 34, 41–70.
- 848 Shchepetkin, A. F. (2015). An adaptive, courant-number-dependent implicit scheme  
 849 for vertical advection in oceanic modeling. *Ocean Modelling*, 91, 38–69.
- 850 Shchepetkin, A. F., & McWilliams, J. C. (2003). A method for computing hor-  
 851 izontal pressure-gradient force in an oceanic model with a nonaligned ver-  
 852 tical coordinate. *Journal of Geophysical Research: Oceans*, 108(C3). doi:  
 853 10.1029/2001JC001047
- 854 Shchepetkin, A. F., & McWilliams, J. C. (2005). The regional oceanic modeling  
 855 system (roms): a split-explicit, free-surface, topography-following-coordinate  
 856 oceanic model. *Ocean Modelling*, 9(4), 347–404. Retrieved from <https://www.sciencedirect.com/science/article/pii/S1463500304000484> doi:  
 857 <https://doi.org/10.1016/j.ocemod.2004.08.002>
- 858 Stewart, K., Hogg, A. M., Griffies, S., Heerdegen, A., Ward, M., Spence, P., &  
 859 England, M. H. (2017). Vertical resolution of baroclinic modes in global  
 860 ocean models. *Ocean Modelling*, 113, 50–65. Retrieved from <https://www.sciencedirect.com/science/article/pii/S1463500317300434> doi:  
 861 <https://doi.org/10.1016/j.ocemod.2017.03.012>
- 862 Stommel, H. (1958). The abyssal circulation. *Deep-Sea Research*, 5(1), 80–82.
- 863 Taylor, G. (1922). Diffusion by continuous movements. *Proc. London Math. Soc.*,  
 864 2(1), 196–212.
- 865 Thakur, R., Arbic, B. K., Menemenlis, D., Momeni, K., Pan, Y., Peltier, W. R., ...  
 866 Ma, Y. (2022). Impact of vertical mixing parameterizations on internal gravity  
 867 wave spectra in regional ocean models. *Geophysical Research Letters*, 49(16),  
 868 e2022GL099614. doi: 10.1029/2022GL099614
- 869 Tozer, B., Sandwell, D. T., Smith, W. H. F., Olson, C., Beale, J. R., & Wessel,  
 870 P. (2019). Global bathymetry and topography at 15 arc sec: Srtm15+.  
 871 *Earth and Space Science*, 6(10), 1847–1864. Retrieved from <https://agupubs.onlinelibrary.wiley.com/doi/abs/10.1029/2019EA000658> doi:  
 872 10.1029/2019EA000658

- 878 https://doi.org/10.1029/2019EA000658  
879 Vic, C., Ferron, B., Thierry, V., Mercier, H., & Lherminier, P. (2021). Tidal and  
880 near-inertial internal waves over the Reykjanes Ridge. *Journal of Physical*  
881 *Oceanography*, 51, 419–437. doi: 10.1175/JPO-D-20-0097.1  
882 Vic, C., Gula, J., Roullet, G., & Pradillon, F. (2018). Dispersion of deep-sea hy-  
883 drothermal vent effluents and larvae by submesoscale and tidal currents. *Deep-*  
884 *Sea Research Part I*, 133, 1–18. doi: 10.1016/j.dsr.2018.01.001  
885 Waterhouse, A. F., MacKinnon, J. A., Nash, J. D., Alford, M. H., Kunze, E., Sim-  
886 mons, H. L., ... others (2014). Global patterns of diapycnal mixing from  
887 measurements of the turbulent dissipation rate. *Journal of Physical Oceanogra-*  
888 *phy*, 44(7), 1854–1872. doi: <https://doi.org/10.1175/JPO-D-13-0104.1>  
889 Xu, X., Chassignet, E. P., & Wallcraft, A. J. (2023). Impact of vertical resolu-  
890 tion on representing baroclinic modes and water mass distribution in the  
891 North Atlantic. *Ocean Modelling*, 186, 102261. Retrieved from <https://www.sciencedirect.com/science/article/pii/S1463500323001014> doi:  
892 <https://doi.org/10.1016/j.ocemod.2023.102261>  
893 Zilberman, N., Becker, J., Merrifield, M., & Carter, G. (2009). Model estimates  
894 of  $M_2$  internal tide generation over Mid-Atlantic Ridge topography. *Journal of*  
895 *Physical Oceanography*, 39(10), 2635–2651. doi: 10.1175/2008JPO4136.1  
896

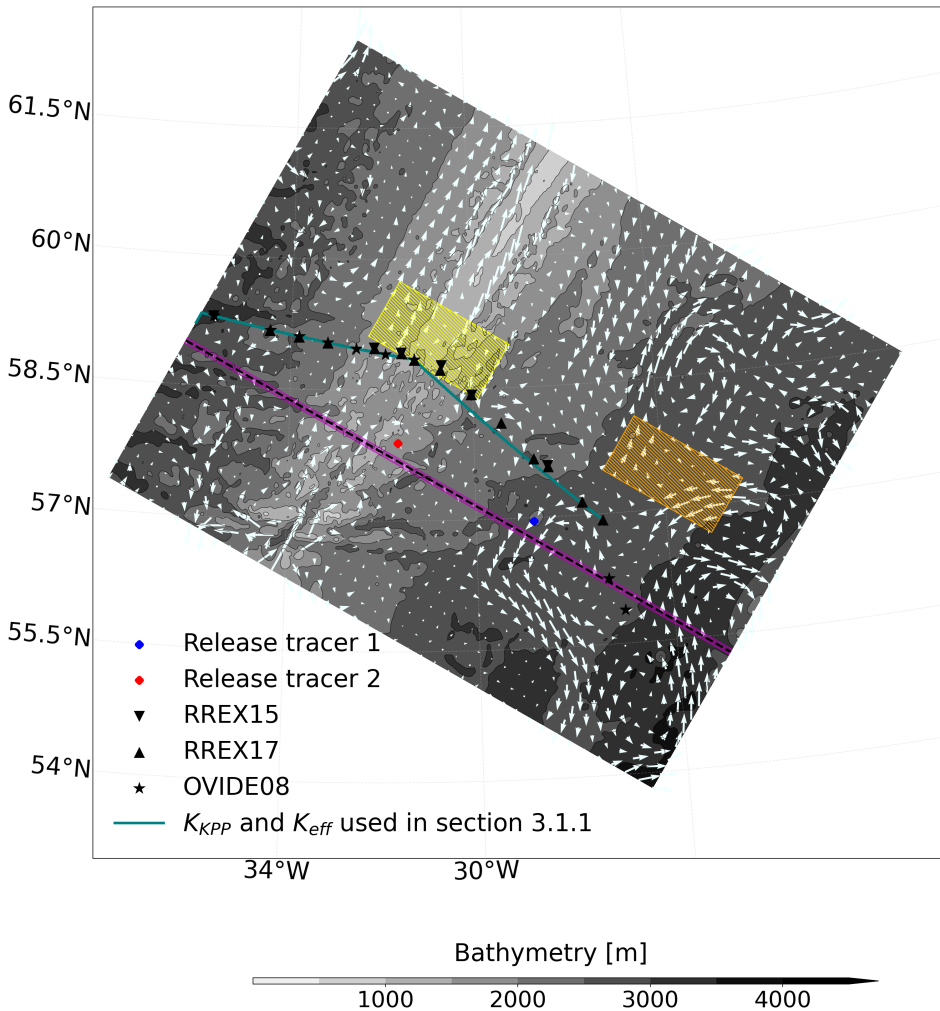


**Figure 3.** Top view of the Reykjanes Ridge and the model grid. Red and blue squares indicate the initial location of the passive tracer patches. Tracer patch 1 is released at  $\rho = 1027.700 \text{ kg m}^{-3}$ , while tracer patch 2 is released at  $\rho = 1027.775 \text{ kg m}^{-3}$ . The arrows represent the circulation at 1000 meters depth averaged over 40 days. The bathymetry of the grid is indicated by the white-black colorbar. The yellow and orange dashed areas are used to contrast the mixing profiles between the ridge and the abyssal plain in section 3.1. The black dashed line is the vertical section used in figures 4, 5 and 8; the purple area represents the along ridge vertical sections used in figures 10 and 11.

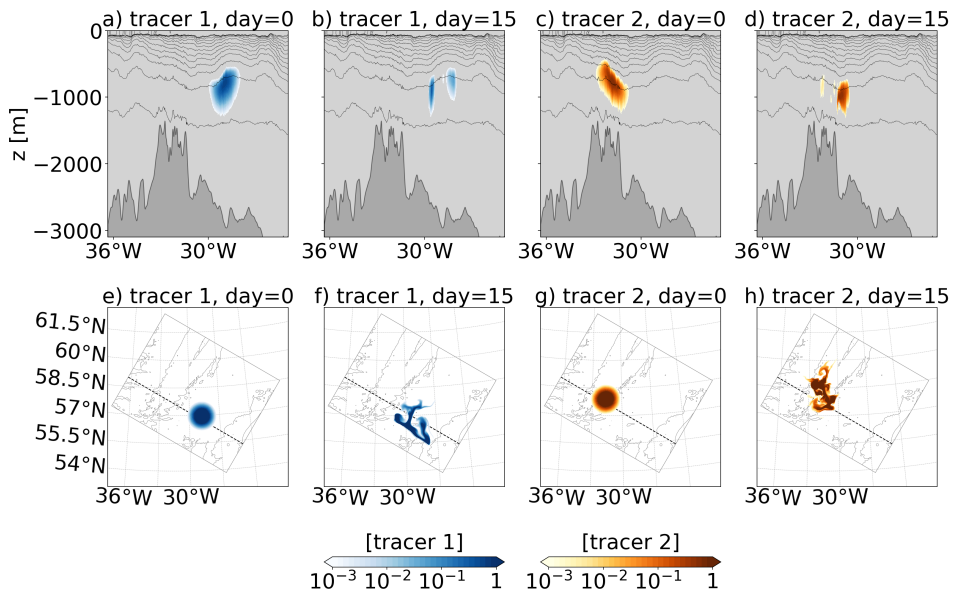


**Figure 4.** Vertical (a-d) and horizontal (e-h) snapshots of tracer concentration from the configuration exp200-rsup5 for a,e) tracer 1 at release, b,f) tracer 1 after 15 days, c,g) tracer 2 at release, and d,h) tracer 2 after 15 days. The solid black lines in the upper panels represent the potential density field referenced at the surface from  $1026.5 \text{ kg.m}^{-3}$  to  $1028.4 \text{ kg.m}^{-3}$  with variations of  $0.1 \text{ kg m}^{-3}$ . The vertical section used is the black dashed line in panels (e-h). Tracer patches are vertically integrated in the lower panels and the solid black lines represent the contour of the bathymetry every 1000 meters.

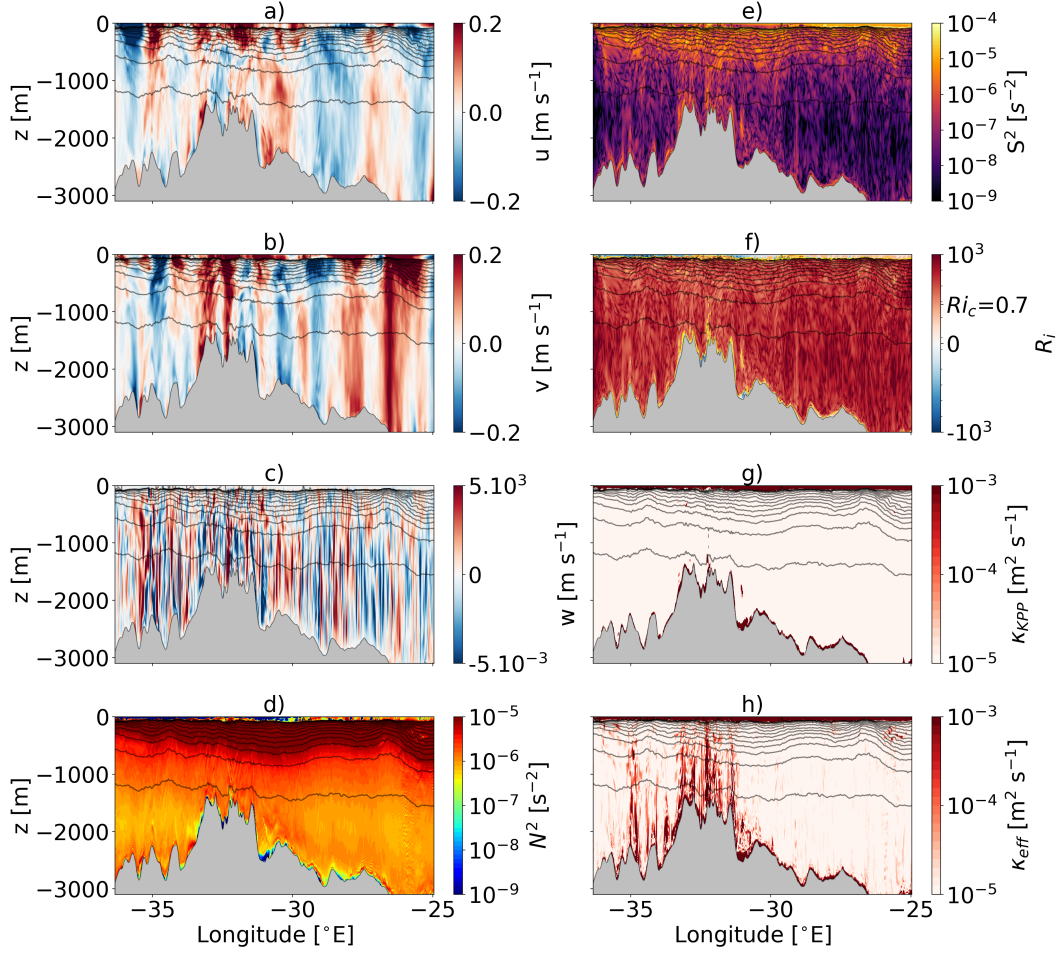


**Figure 5.** Vertical section of (a) zonal velocity  $u$  (in m/s), (b) meridional velocity  $v$  (in m/s), (c) vertical velocity  $w$  (in m/s), (d) Brunt-Vaisala frequency  $N^2$  (in  $s^{-2}$ ), (e) vertical shear of horizontal velocity  $S^2$  (in  $s^{-2}$ ), (f) Richardson number  $Ri_c$ , (g) the parameterised mixing  $K_{KPP}$ , and (h) the effective mixing  $K_{eff}$  for the exp200-rsup5 experiment 10 days after tracer release. The solid black lines in the upper panels represent the potential density field referenced at the surface from  $1026.5 \text{ kg.m}^{-3}$  to  $1028.4 \text{ kg.m}^{-3}$  with variations of  $0.1 \text{ kg m}^{-3}$ . The vertical section is taken at the black dashed line in figure 3.

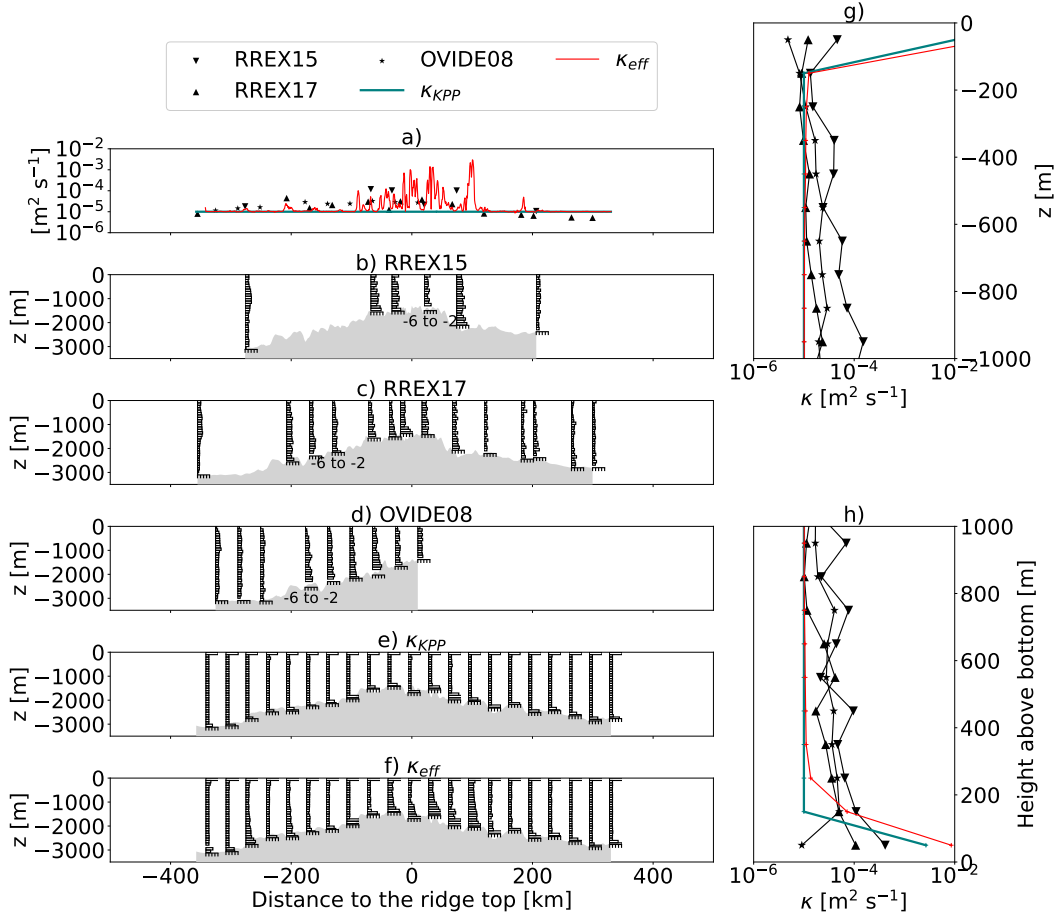


**Figure 6.** Comparison of observed diffusivities from campaigns RREX15, RREX17, and OVIDE08, with parameterized diffusivities from KPP and effective diffusivity  $K_{eff}$  in the exp200-rsup5 configuration along the blue section visible in figure 3. Median diffusivities as a function of (a) the distance to the ridge, (g) the depth and (h) the height above bottom for the RREX15, RREX17 and OVIDE08 campaigns, the KPP diffusivity, and the effective diffusivity  $K_{eff}$ . The median is computed over 29 days for  $K_{KPP}$  and  $K_{eff}$ . Vertical profiles of diffusivities estimated from (b) RREX15 (c) RREX17, and (d) OVIDE08 observations. Median values from 29 days of exp200-rsup5 for (e) the KPP diffusivity and (f) the effective diffusivity  $K_{eff}$ . The vertical profiles are shown every 20km in panels e) and f).

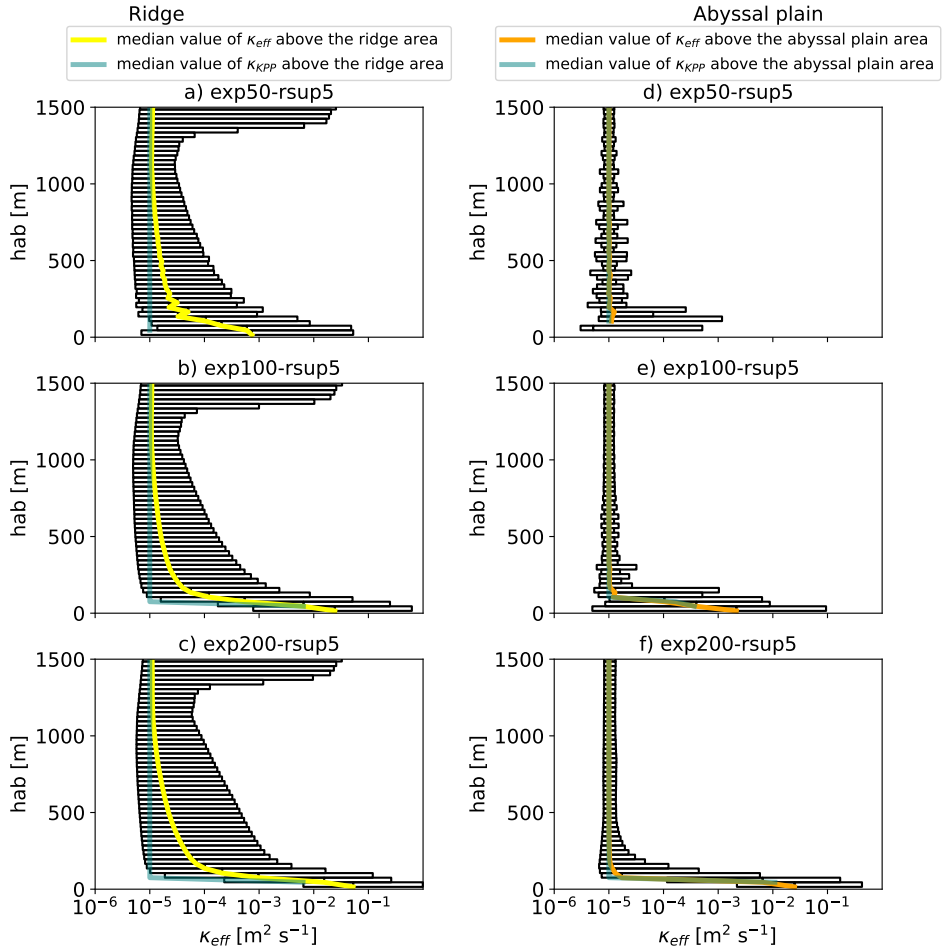


**Figure 7.** Effective mixing  $K_{eff}$  as a function of height above bottom averaged over (a,b,c) the ridge (yellow dashed rectangle on Fig. 3), and (d,e,f) the abyssal plain (orange dashed rectangle on Fig. 3) for configurations (a,d) exp50-rsup5, (b,e) exp100-rsup5, and (c,f) exp200-rsup5. The edges of the box represent the 10th and the 90th percentiles of  $K_{eff}$  for each height above bottom.

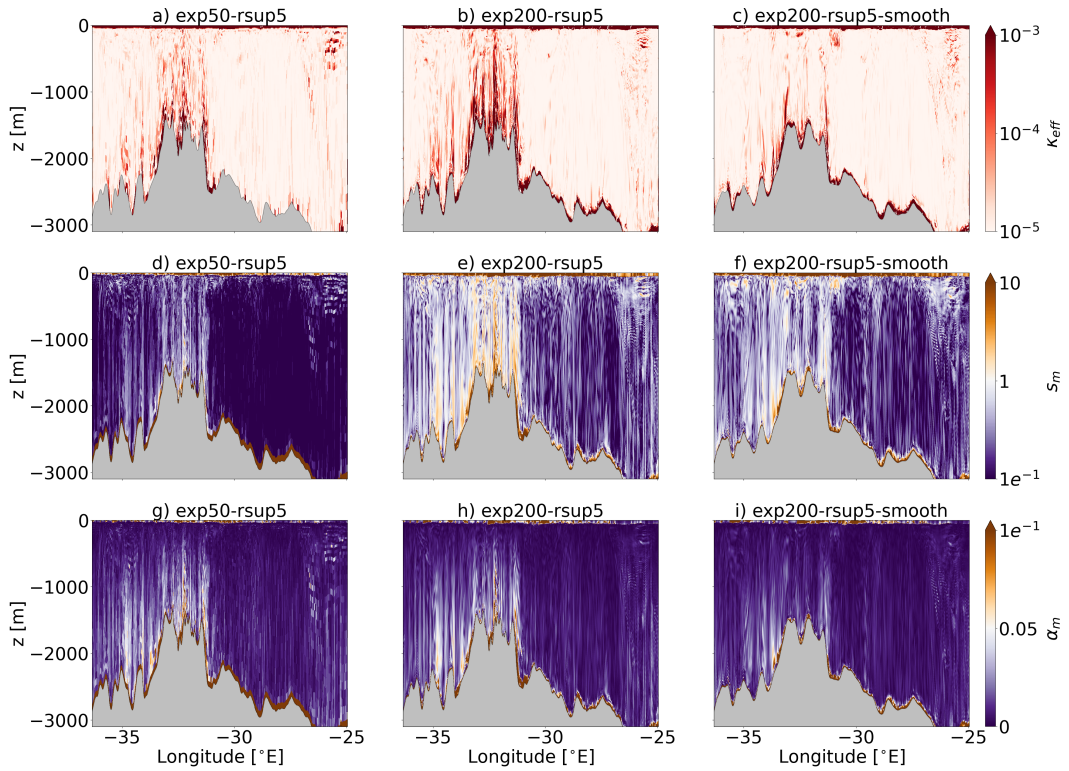


**Figure 8.** Snapshot at 10 days of vertical sections of (a-c)  $K_{eff}$ , (d-f) the grid slope ratio  $s_m$ , and (g-i) the maximum isopycnal slope  $\alpha_m$ , for (a,d,g) exp50-rsup5, (b,e,h) exp200-rsup5, and (c,f,i) exp200-rsup5-smooth. The values  $\alpha = 0.05$  and  $s_m = 1$  are the critical values  $\alpha_m$  and  $s_m$ . The vertical section is taken at the black dashed line in figure 3.

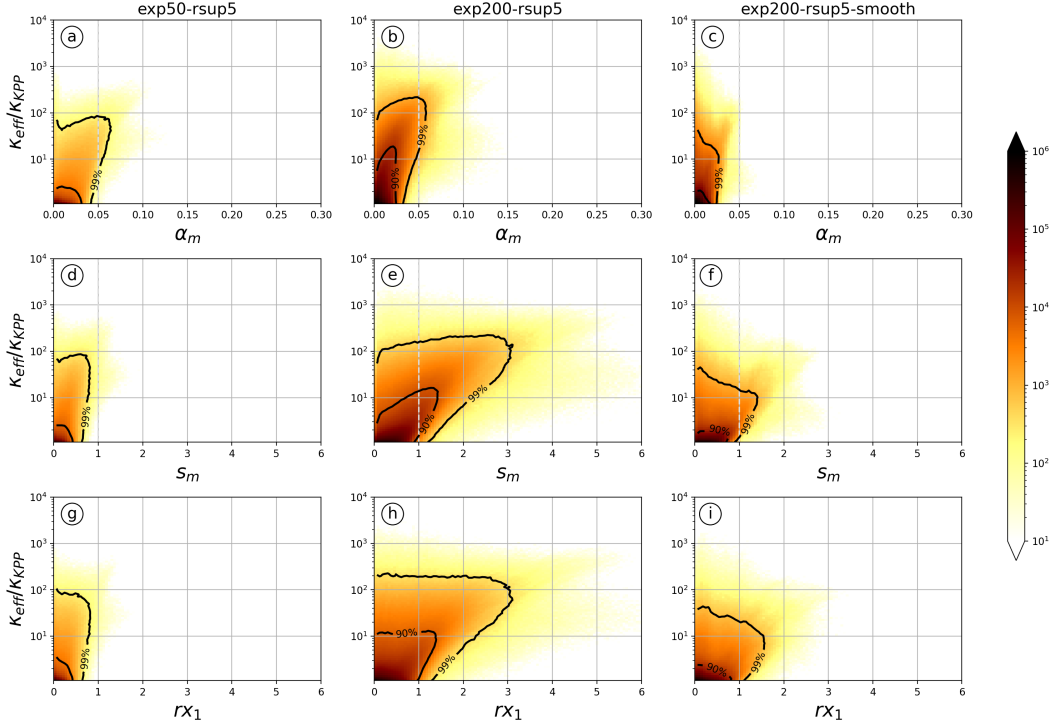


**Figure 9.** Binned statistics for the ratio of the time mean effective and parameterized mixing versus (a-c) the isopycnal slope  $\alpha_m$ , (d-f) the grid slope ratio  $s_m$ , and (g-i) the hydrostatic consistency condition  $rx_1$ , for (a,d,g) exp50-rsup5, (b,e,h) exp200-rsup5, and (c,f,i) exp200-rsup5-smooth. The dashed grey lines show the critical values for the isopycnal slope and grid slope ratio. The black contour are the integrated domains containing 90% and 99% of the points.

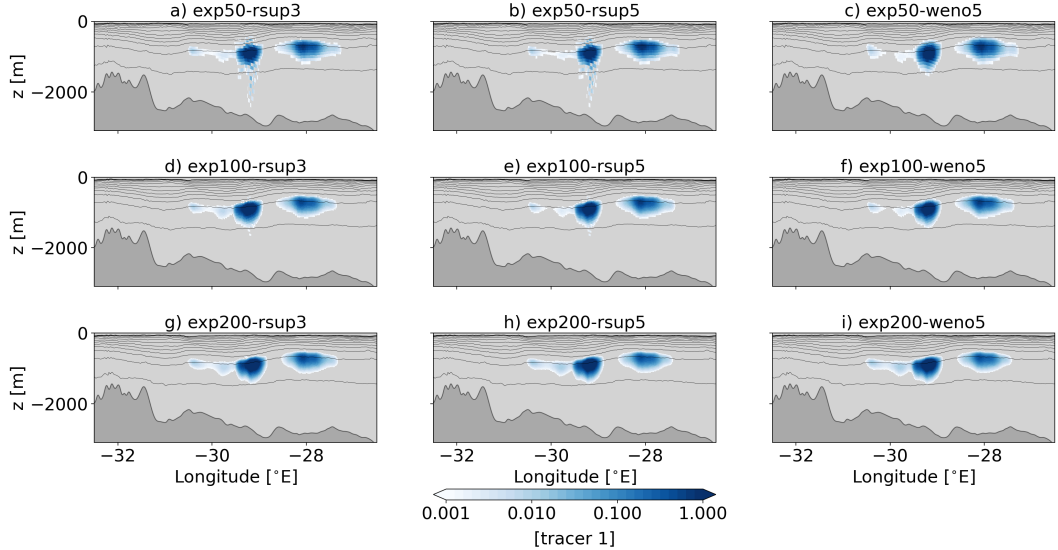


**Figure 10.** Vertical section of tracer 1 after 10 days for each configuration. The tracer patch is summed over 10 grid points in the along ridge direction indicated by the purple area in figure 3 and negative concentrations are not shown.

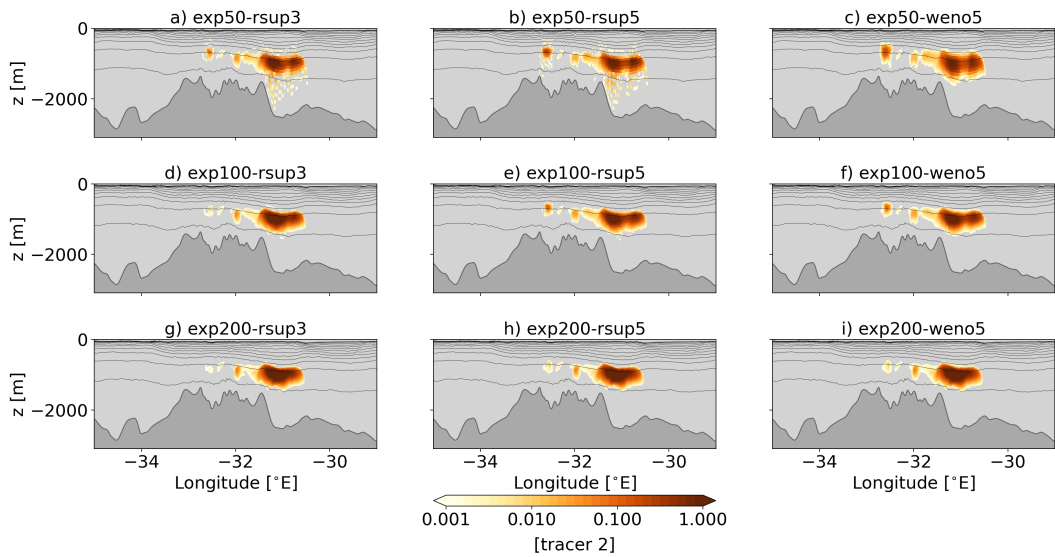


**Figure 11.** Vertical section of tracer 2 after 10 days for each configuration. The tracer patch is summed over 10 grid points in the along ridge direction. The location of the section corresponds to the purple area in figure 3 and negative concentrations are not shown.

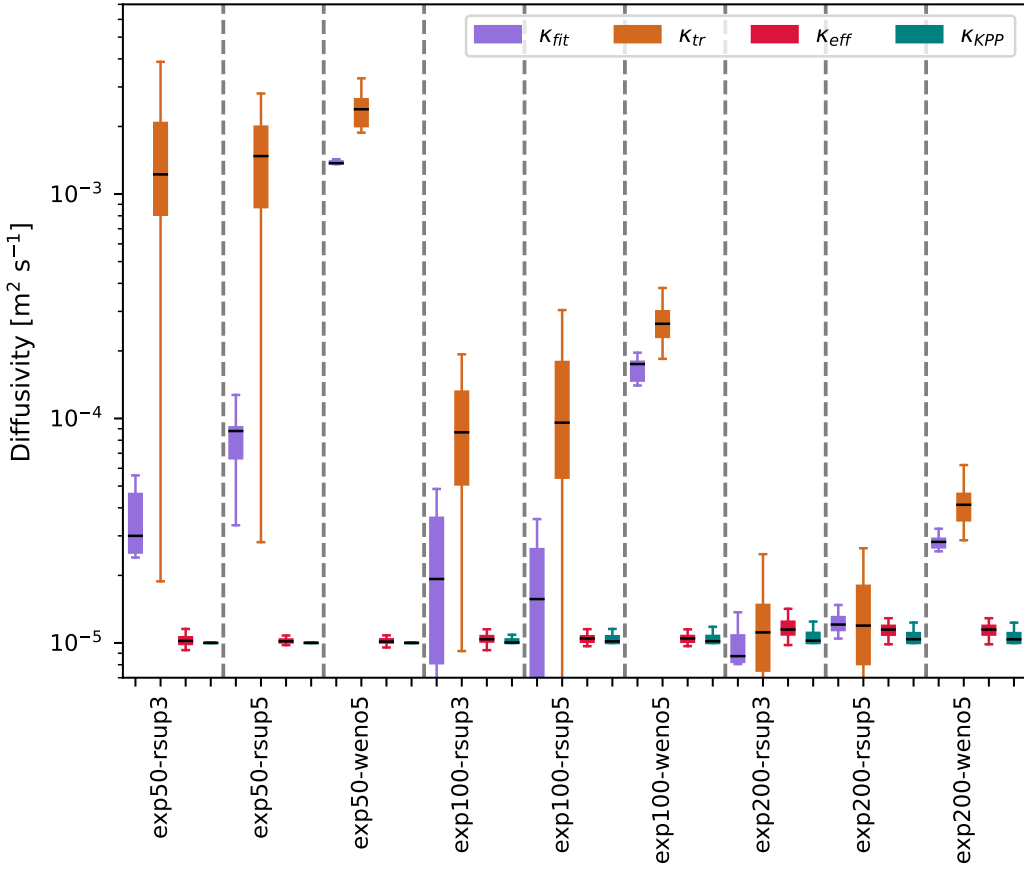


**Figure 12.** Estimation of the diffusivities experienced by tracer 1 for configurations exp50-rsup3, exp50-rsup5, exp50-rweno5, exp100-rsup3, exp100-rsup5, exp100-rsweno5, exp200-rsup3, exp200-rsup5, exp200-rsweno5. The parameterised diffusivity  $K_{KPP}$  is in blue, the online diagnosed effective diffusivity  $K_{eff}$  is in red, and the two tracer-based diffusivities  $K_{tr}$  and  $K_{fit}$  are in orange and purple.  $K_{eff}$  and  $K_{KPP}$  are weighted by the tracer concentration following Equ. 3. Diffusivities are considered for the first 15 days. For each box plot, the extremities of the box represent the minimum and the maximum values of the distribution and the box shows the first quartile, the median and the third quartile of the distribution. Concentrations of tracer less than  $1e-6 \text{ m}^2 \text{ s}^{-1}$  are ignored in the calculation of diffusivities.  $K_{fit}$  is considered on the last 10 days because it encounters time adjustment on the first 5 days (see fig. 13).

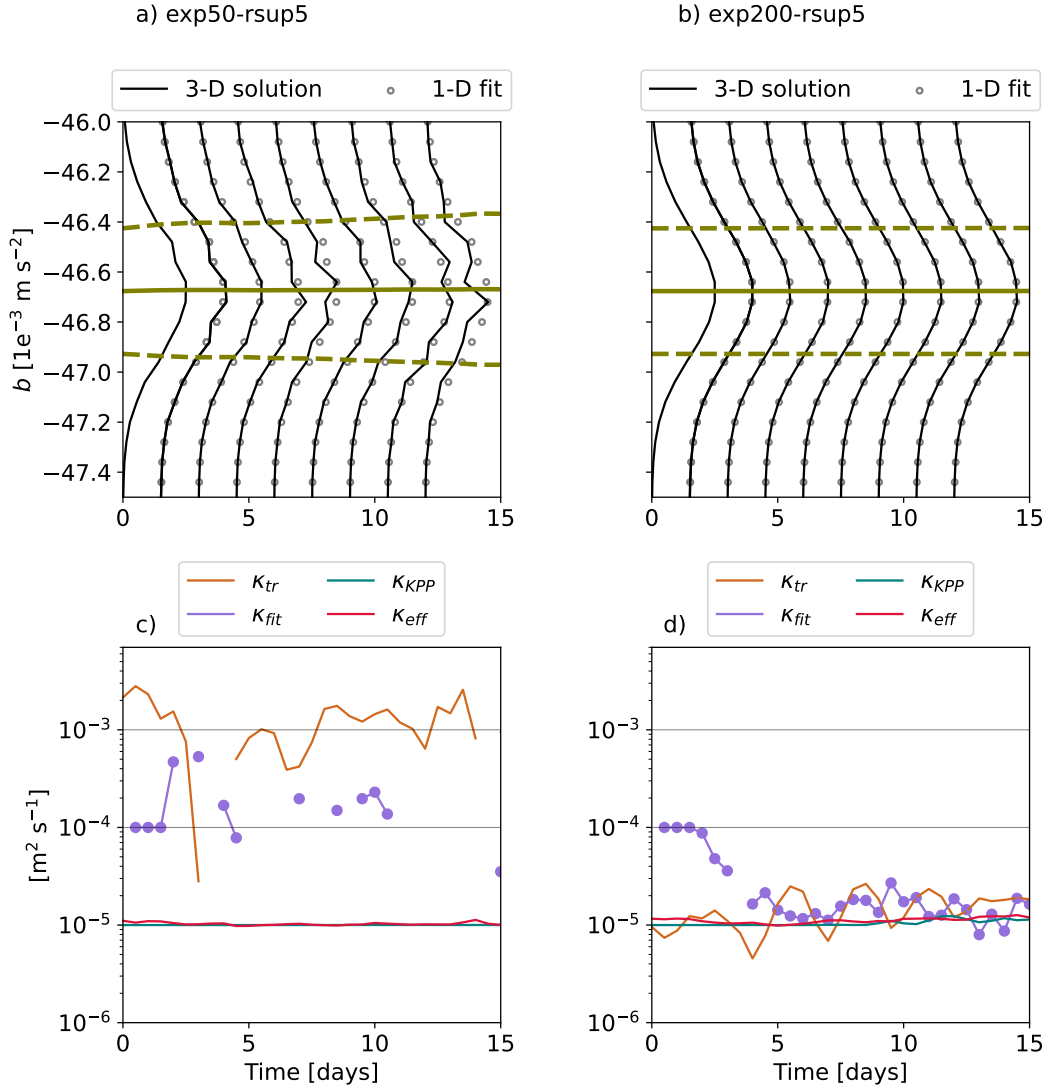


**Figure 13.** a,b) tracer 1 concentration binned in buoyancy space (black line) and one-dimensional fit used to compute  $K_{fit}$  (dot markers) for configurations a) exp50-rsup5 and b) exp200-rsup5. Green lines show the centre of gravity (plain) and the standard deviation (dashed) for the one-dimensional fit (equation 4). The lower panels show for configurations c) exp50-rsup5 and d) exp200-rsup5 the time evolution of diffusivities experienced by tracer 1: the parameterised diffusivity  $K_{KPP}$  (blue line), the online diagnosed effective diffusivity  $K_{eff}$  in red, and the offline diagnosed effective diffusivities  $K_{tr}$  and  $K_{fit}$  (orange and purple lines). Concentrations of tracer less than  $1\text{e-}6$  are not considered here.

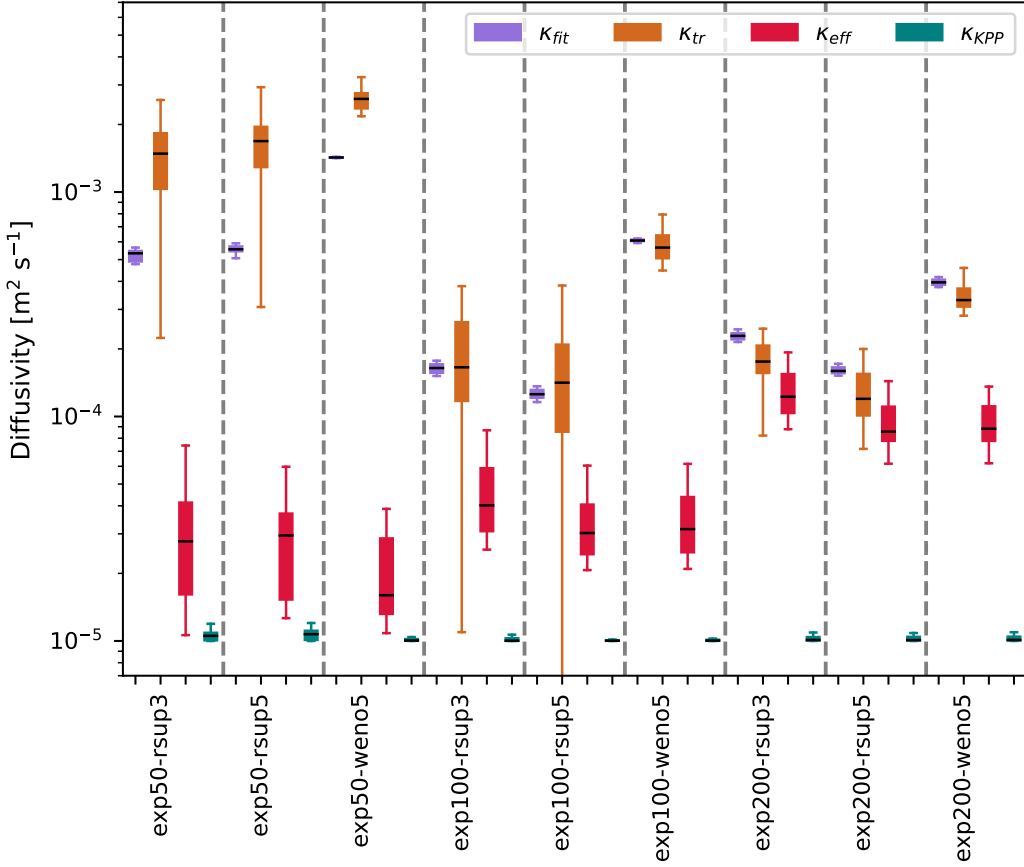


**Figure 14.** Estimation of the diffusivities experienced by tracer 2 for configurations  $\text{exp50-rsup3}$ ,  $\text{exp50-rsup5}$ ,  $\text{exp50-rweno5}$ ,  $\text{exp100-rsup3}$ ,  $\text{exp100-rsup5}$ ,  $\text{exp100-rweno5}$ ,  $\text{exp200-rsup3}$ ,  $\text{exp200-rsup5}$ ,  $\text{exp200-rweno5}$ . The parameterised diffusivity  $K_{KPP}$  is in blue, the online diagnosed effective diffusivity  $K_{eff}$  is in red, and the two tracer-based diffusivities  $K_{tr}$  and  $K_{fit}$  are in orange and purple.  $K_{eff}$  and  $K_{KPP}$  are weighted by the tracer concentration following Equ. 3. Diffusivities are considered for the first 15 days. For each box plot, the extremities of the box represent the minimum and the maximum values of the distribution and the box shows the first quartile, the median and the third quartile of the distribution. Concentrations of tracer less than  $1\text{e-}6 \text{ m}^2 \text{ s}^{-1}$  are ignored in the calculation of diffusivities.  $K_{fit}$  is considered on the last 10 days because it encounters time adjustment on the first 5 days (see fig. 13).

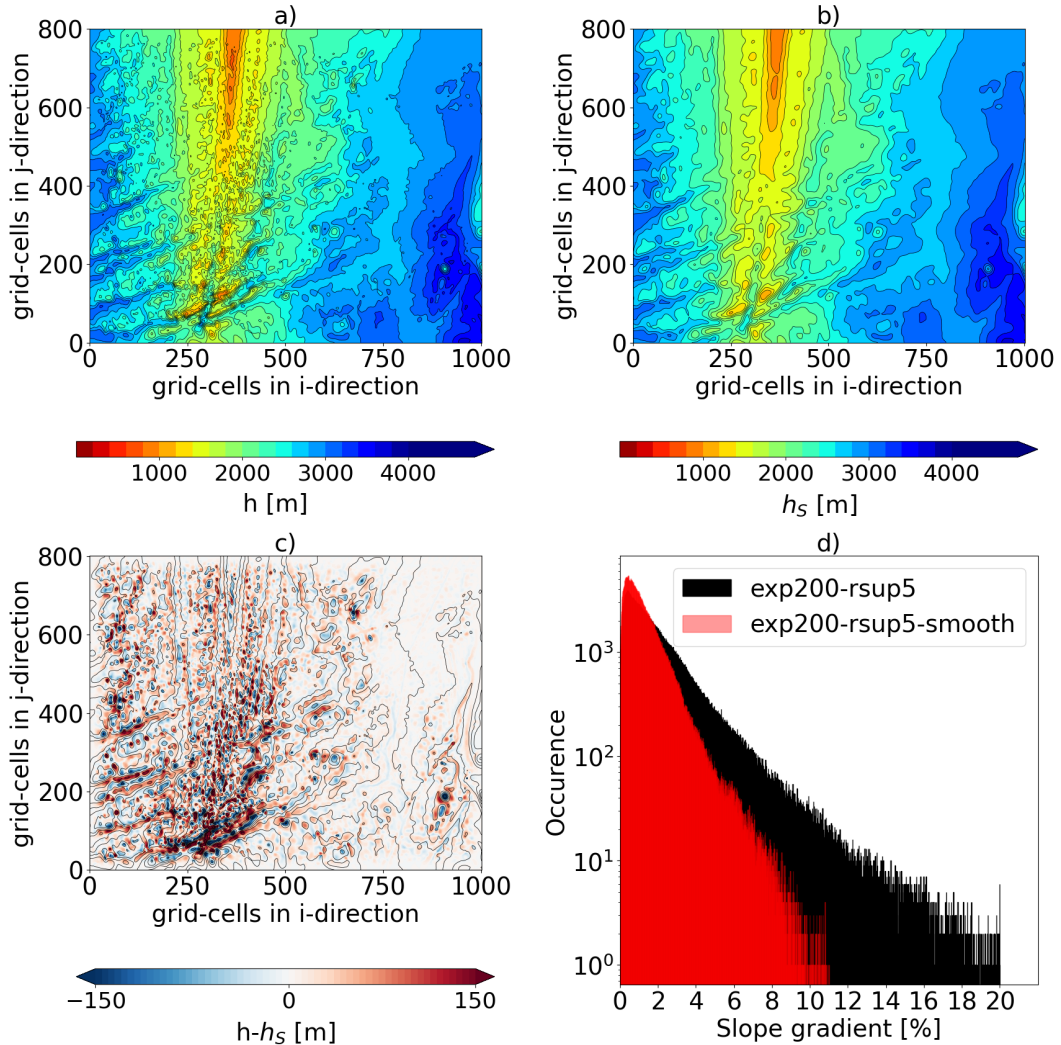


**Figure 15.** (a) Reference bathymetry and (b) smoothed bathymetry used in exp-200-rsup5-smooth (c) difference between reference and smoothed bathymetries and (d) histogram of the slope gradient with the unsmoothed topography displayed over the exp200-rsup5 configuration (black histogram) and the smoothed topography used in the exp200-rsup5-smooth configuration (light red histogram). The black lines are the contour each 200m of the reference bathymetry (panels a) and c)) and of the smoothed bathymetry (panel b)).

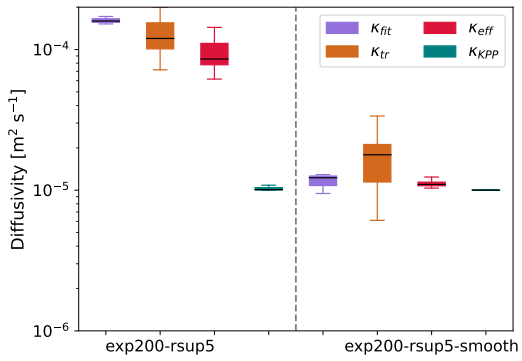


**Figure 16.** Diffusivities experienced by tracer 2 for configurations  $\text{exp200-rsup5}$  and  $\text{exp200-rsup5-smooth}$ . The parameterised diffusivity  $K_{KPP}$  is in blue, the effective diffusivity  $K_{eff}$  is in red, and the two tracer-based diffusivities  $K_{tr}$  and  $K_{fit}$  are in orange and purple.  $K_{eff}$  and  $K_{KPP}$  are weighted by the tracer concentration following Equ. 3. Diffusivities are considered for the first 15 days. For each box plot, the extremities of the box represent the minimum and the maximum values of the distribution and the box shows the first quartile, the median and the third quartile of the distribution. Concentrations of tracer less than  $1\text{e-}6 \text{ m}^2 \text{ s}^{-1}$  are not considered when computing diffusivities.  $K_{fit}$  is considered on the last 10 days because it encounters time adjustment on the first 5 days (see fig. 13).

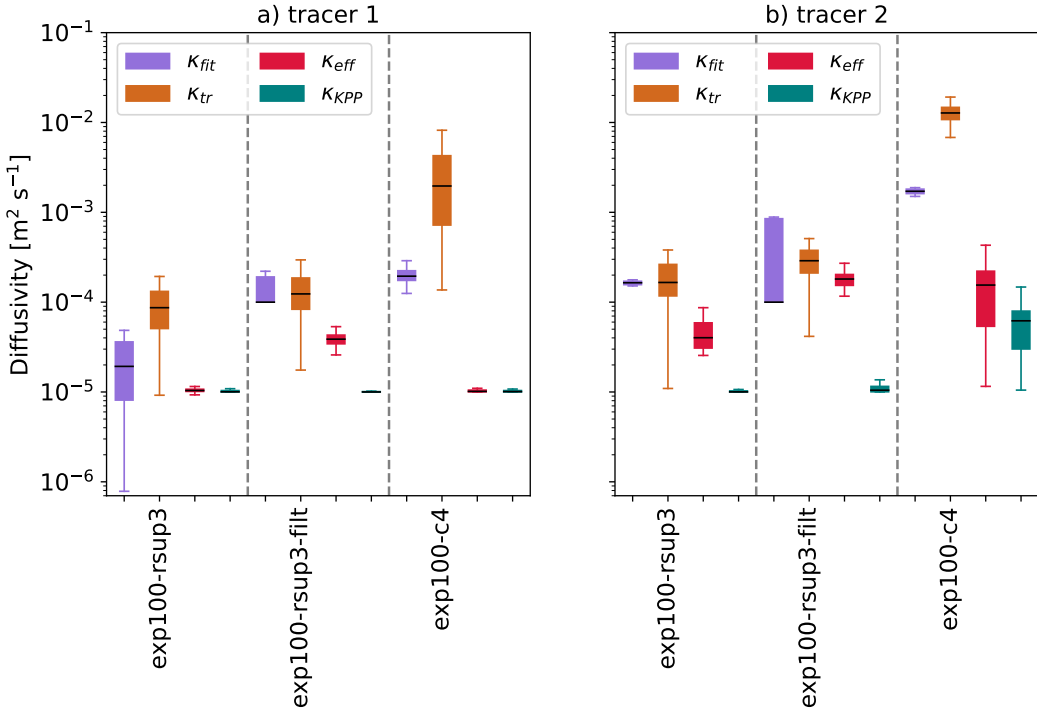


**Figure A1.** Estimation of the diffusivities experienced by a) the tracer 1 and b) the tracer 2 for configurations exp100-rsup3, exp100-rsup3-filt and exp100-c4. The parameterised diffusivity is in blue, the effective diffusivity  $K_{eff}$  is in red, and the two tracer-based diffusivities  $K_{tr}$  and  $K_{fit}$  are in orange and purple.  $K_{eff}$  and  $K_{KPP}$  are weighted by the tracer concentration following Equ. 3. Diffusivities are considered for the first 15 days. For each box plot, the extremities of the box represent the minimum and the maximum values of the distribution and the box shows the first quartile, the median and the third quartile of the distribution. Concentrations of tracer less than  $1e-6 \text{ m}^2 \text{ s}^{-1}$  are not considered when computing diffusivities.  $K_{fit}$  is considered on the last 10 days.